Marine and Petroleum Geology 164 (2024) 106790



Contents lists available at ScienceDirect

Marine and Petroleum Geology

journal homepage: www.elsevier.com/locate/marpetgeo

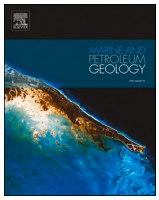



# Petroleum accumulations in the tarim basin during various tectonic stages as revealed by U–Pb dating of multi-phase calcite veins in deeply buried carbonate reservoirs

Hao Xu [a], Zicheng Cao [b], Lili Gui [c], Kamaldeen O. Omosanya [d], Feng Geng [b], Ze Tao [a], Xiaowen Guo [a,*]

[a] Key Laboratory of Tectonics and Petroleum Resources, Ministry of Education, China University of Geosciences, Wuhan, 430074, China
[b] Northwest Oilfield Company, SINOPEC, Xinjiang, 830011, China
[c] Key Laboratory of Basin Structure and Hydrocarbon Accumulation, CNPC, Beijing, 100083, China
[d] Department of Geology and Geophysics, Oasisgeokonsult, 7052, Trondheim, Norway

ARTICLE INFO

*Keywords:*
Deeply buried carbonate reservoirs
Calcite U–Pb geochronology
Fluid flow and oil-charging
Hydrothermal activity

ABSTRACT

Significant discoveries in deeply buried marine carbonate petroleum exploration have been made recently in the Tarim Basin, NW China. Constraining the evolutionary history of fluid activity and the process of oil charging in the deeply buried carbonate reservoirs is crucial for further hydrocarbon exploration and development. In this study, we conducted an integrated study combining petrography, geochemistry, fluid inclusion analysis, and in-situ U–Pb dating of multi-phase calcite veins collected from the Ordovician carbonate reservoirs, Akeyasu area, Tarim Basin. Four distinct phases of calcite veins were found within the Ordovician carbonate reservoirs. The U–Pb ages of these four phases of calcite veins are as follows: 459.8 ± 4.7 Ma, 418.8 ± 3.7 Ma, 329.7 ± 1.6 Ma to 310.0 ± 3.6 Ma, and 291.7 ± 6.1 Ma to 220.5 ± 7.3 Ma. These ages closely correspond to key tectonic events that influenced the study area, specifically, the Middle Caledonian, Late Caledonian, Middle Hercynian, and Late Hercynian orogenies, respectively. The first phase (C1) calcite veins are believed to have precipitated from meteoric water, closely associated with the first episode of oil charging. Phase II (C2) calcite veins primarily formed from Early-Middle Ordovician formation water. Phase III and phase IV (C3 and C4) calcite veins originated from Middle-Late Cambrian formation water and hydrothermal fluids, respectively. Significantly, the second and third episodes of oil charging occurred concurrently with the precipitation of C3 and C4 calcites. Seismic data analysis of Paleozoic strata in the Akeyasu area revealed four stages of fault activity, corresponding to the Early Caledonian, Middle Caledonian, Late Caledonian-Early Hercynian, and Middle-Late Hercynian orogenies. Our findings strongly suggest that the evolution of fluid activity and oil charging was primarily governed by regional orogeny. These large-scale tectonic shifts led to intensified fault activity, ultimately controlling fluid activity and oil charging dynamics. Furthermore, this intensified faulting eased the connection between deep fluid systems and the Ordovician carbonate reservoirs, serving as the primary conduits for fluid migration and oil charging within the deeply buried Ordovician carbonate reservoirs.

## 1. Introduction

Deeply buried carbonate reservoirs have garnered increasing global attention in recent oil and gas exploration and development efforts. In the Tarim Basin, NW China, petroleum pools have been discovered at depths exceeding 8000 m, suggesting significant economic potential in the exploitation of deep-buried carbonate reservoirs in the region (Lei et al., 2021). Oil and gas within carbonate reservoirs primarily occupy complex fracture-cavity systems formed through epigenetic dissolution, burial, and hydrothermal alterations (Kerans, 1988; Moore and Wade, 2013; He et al., 2017, 2021). Fluid flow plays a fundamental role in pore development within carbonate reservoirs and is closely linked to petroleum migration and accumulation. As a result, understanding the evolution of fluids in petroleum-bearing basins can help constrain the processes of petroleum migration and accumulation.

The Akeyasu area is a typical Oil field with reservoirs dominantly

* Corresponding author.
*E-mail address:* cuggxw@163.com (X. Guo).

https://doi.org/10.1016/j.marpetgeo.2024.106790
Received 25 October 2023; Received in revised form 28 February 2024; Accepted 4 March 2024
Available online 17 March 2024
0264-8172/© 2024 Published by Elsevier Ltd.

composed of deeply buried marine carbonate rocks. Oil fields in the Akeyasu area of the Tarim Basin have undergone multi-stage hydrocarbon accumulation processes (Wang et al., 2023; Xu et al., 2021). Significant progress has been made in understanding the Ordovician reservoirs, which lie at burial depths ranging from 5500 m to 7300 m. Crude oils primarily exist within the pores, fractures, and caves of deeply buried carbonate reservoirs (Yun, 2008; Jin et al., 2016). Earlier studies in the Akeyasu area have predominantly focused on the petrographic and geochemical characteristics of the Ordovician carbonate reservoirs. These studies have found three types of diagenetic fluids: Meteoric, formation and hydrothermal fluids (Han et al., 2019; Chen et al., 2022a). However, the specific phases and origins of vein-forming fluids,

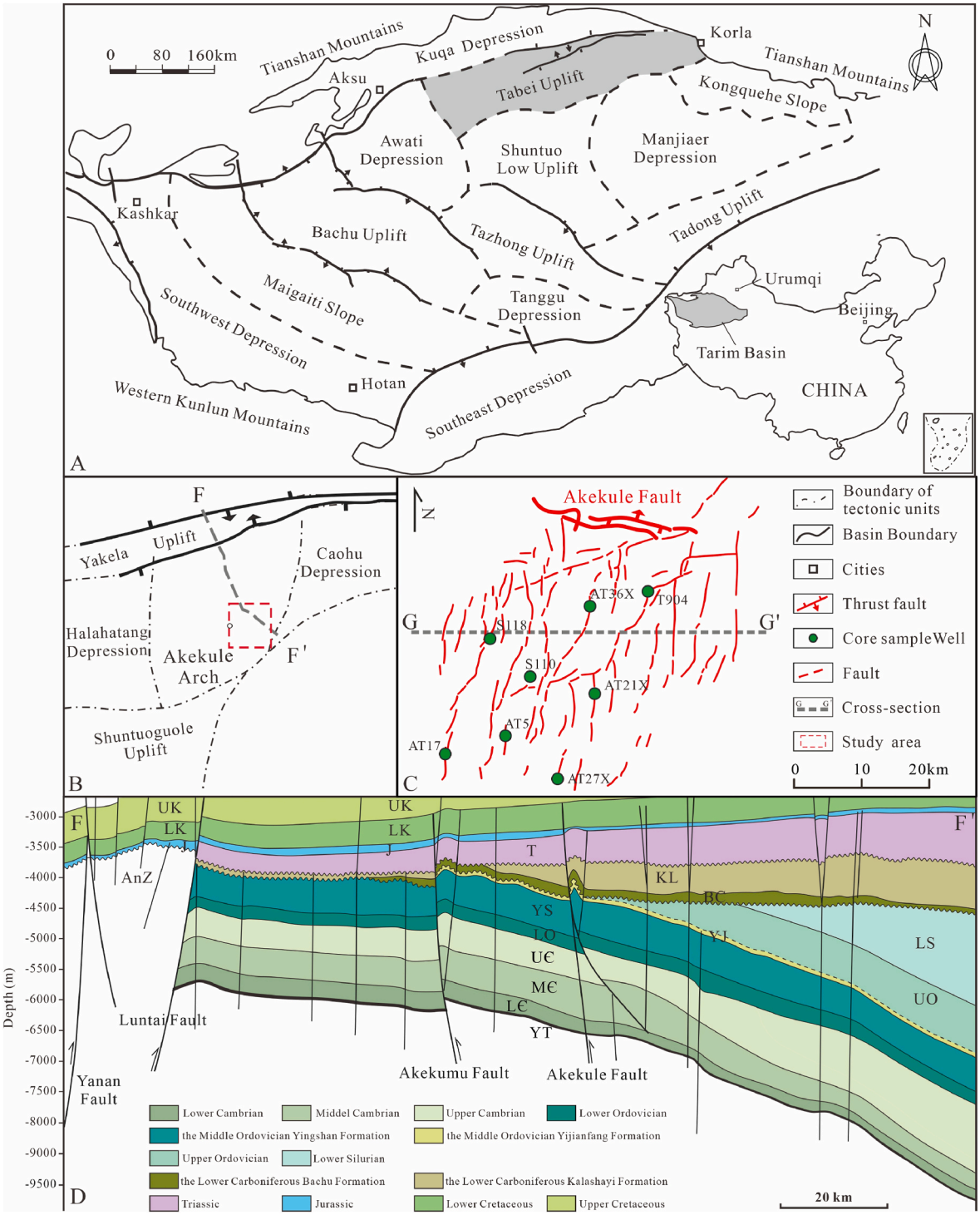


**Fig. 1.** A: The main structural units in the Tarim Basin and the location of the Tabei Uplift, Tarim Basin, China. B: Location of the study area on the Akekule Arch. C: A regional map highlighting the location of faults and wells sampled in the Akeyasu area. Faults are projected to the top of the Middle Ordovician. D: Cross-section FF' showing the structural framework, major stratigraphic sequences and faults of the Tabei Uplift. UK—Upper Cretaceous, LK—Lower Cretaceous; J—Jurassic; T—Triassic; KL—the Lower Carboniferous Kalashayi Formation, BC—the Lower Carboniferous Bachu Formation; LS—Lower Silurian; UO—Upper Ordovician, YJ—the Middle Ordovician Yijianfang Formation, YS—the Middle Ordovician Yingshan Formation, LO—Lower Ordovician; UЄ—Upper Cambrian, MЄ—Middle Cambrian, LЄ—Lower Cambrian, YT—the Lower Cambrian Yuertusi Formation.

the timing of diagenetic events, as well as the evolution of fluids, its relationship with the regional tectonic evolution and the petroleum accumulation process remain unclear.

Calcite precipitation resulting from fluid flow events in sedimentary basins record crucial geological information (such as temperature, pressure, salinity and Redox environment) about paleo-fluids (Smith et al., 1991; Lottermoser, 1992; Guo et al., 2016; Yang et al., 2022a; Cruset et al., 2023). Geochemical properties and dating of different phases of calcite can reveal the complex fluid evolution history within petroleum systems (Cruset et al., 2021; Rochelle-Bates et al., 2020; Chen et al., 2022a; Cong et al., 2022). Investigating the origin of vein-forming fluids and the absolute age of diagenetic minerals is essential for understanding fluid flow behavior within carbonate reservoirs (Han et al., 2019; Dewever et al., 2010). Geochemical analysis of calcite, including rare earth elements (REEs), as well as isotopic features such as $^{13}C$, $^{18}O$, and $^{87}Sr/^{86}Sr$, can effectively trace the origin of vein-forming fluids (Klein and Beukes, 1989; Bau, 1991; Shields and Stille, 2001; McArthur, 1994; Shields et al., 2003; Bolhar et al., 2004; Bolhar and Van Kranendonk, 2007; Liu et al., 2023; Sun et al., 2023). While fluid inclusion microthermometry combined with burial and thermal history has its limitations in estimating precise paleo geothermal gradients, the new isotopic dating technique, in-situ U–Pb dating by laser ablation-inductively coupled plasma mass spectrometry (LA-ICP-MS), has shown promise in accurately determining the radiometric ages of carbonate minerals (Li et al., 2014; Coogan et al., 2016; Roberts and Walker, 2016; Nuriel et al., 2017; Chen et al., 2022a; Cao et al., 2023). Thus, the absolute timing of calcite precipitation can constrain the absolute timing of the fluid flow events and provide critical chronological constraints on the complex fluid evolution history.

To gain a deeper understanding of fluid evolution and the petroleum accumulation process associated with the tectonics in the deeply buried Ordovician carbonate reservoirs, this paper aims to.

1. Investigate the phases and origins of fluid flow events through petrography, REEs, $^{13}C$, $^{18}O$, and $^{87}Sr/^{86}Sr$ isotopic analysis of calcite veins, and determine the absolute age of calcite veins using the in-situ U–Pb dating technique.
2. Establish the relationship between fluid flow and the history of oil charging based on the correlation between different phases of calcite veins and associated oil inclusions.
3. Summarize the relationships between the tectonics and fluid flow, as well as the history of oil charging in the deeply buried Ordovician carbonate reservoirs of the Akeyasu area.

## 2. Geological setting

The Tarim Basin, situated in northwest China, serves as a typical superimposed petroliferous basin covering approximately 56,000 square kilometers. Within this basin lies the Akeyasu area, situated in the southern limb of the Akekule Arch of Tabei Uplift in the northern region of the Tarim Basin (see Fig. 1). The Akeyasu area holds significant importance as part of the Tahe Oilfield, boasting abundant resources with over 1.1 billion barrels of crude oil potential. The Tabei Uplift is geographically bounded by the Halahatang Sag to the east, the Caohu Sag to the west, the Shuntuoguole Lower Uplift to the south, and the Yakela Uplift to the north (see Fig. 1B).

The Tarim Basin underwent two significant stages of tectonic evolution: the Paleozoic craton basins and the Meso-Cenozoic foreland basins (Jia and Wei, 2002). Throughout the geological history of the Akeyasu area, four important regional tectonic evolution stages have been documented (Wu et al., 2021; Yang et al., 2022a, 2022b). During the Middle Caledonian to Early Hercynian orogeny, there were multiple phases of regional uplift in the northern part of the Akekule Arch. This led to the erosion of Upper Ordovician and Silurian strata and aided significant weathering and karstification processes that had a profound impact on the alteration of Ordovician carbonate reservoirs, thus influencing the reservoir development in the Akeyasu area (Han et al., 2019; Wu et al., 2021). Subsequently, during the late Hercynian to Indosinian orogeny, the regional compression orientation shifted from NNW-SSE to N–S, resulting in the formation of anticlines and E-W-oriented faults that disrupted sedimentation and led to the erosion of upper Carboniferous and Permian strata (Wu et al., 2021). During the Permian period, volcanic hydrothermal activity, potentially influenced by mantle plume activity, further contributed to altering the storage capacity of the Ordovician reservoirs (Jin et al., 2013). The Yanshanian orogeny introduced NE-SW compression stress, resulting in the formation of strike-slip faults and the commencement of continental sediment deposition in the Triassic (Shi, 2020). Finally, the Himalayan orogeny brought significant changes to the Mesozoic-Cenozoic geomorphology of the Akeyasu area, driven by rapid subsidence in the Kuqa Depression in the northwestern part of the Tarim Basin (Yun, 2008). This complex tectonic history in the Tarim Basin gave rise to multiple stages of fluid flow events in the Akeyasu area, further shaping its geological evolution. In map view, most of the faults show a segmented geometry rather than large-scale continuous strike-slip faults (Fig. 1C). Two sets of conjugate strike-slip fault arrays, one trending north-northeast to south-north and the other northeast-east, along with thrust faults trending east-west, are clear (Fig. 1C). High-angle strike-slip faults primarily formed during the early stages, with thrust faults forming after, particularly after the Late Hercynian (Deng et al., 2022).

The Ordovician carbonate reservoirs underwent multiple tectonic uplift events, primarily under the influence of significant compressive stress during the Middle Caledonian to Early Hercynian orogenies. Prolonged exposure led to weathering, leaching of Ordovician strata, and meteoric dissolution (Liu et al., 2021; Han et al., 2019). Notably, the Tarim Basin experienced four distinct periods of volcanic activity during the Sinian-Cambrian, early Ordovician, Permian, and Cretaceous periods. The Tabei Uplift was part of the early Permian Tarim large igneous province (Tian et al., 2010; Jin et al., 2013), and this period of volcanic activity, combined with hydrothermal fluids associated with hydrocarbons, likely eased upward migration through fault-fracture systems. These processes are recorded by the calcite veins found within the reservoirs (Jin et al., 2013).

Sedimentary successions in the Akeyasu area span from Cambrian marine carbonates to Quaternary terrestrial clastic sediments, with a total thickness reaching up to 10,000 m (see Fig. 1D). The Ordovician strata can be divided into six stratigraphic units from bottom to top: the Penglaiba, Yingshan, Yijianfang, Qiaerbake, Lianglitage and the Sangtamu Formation (see Fig. 2). Among these, the Yingshan and Yijianfang Formations serve as the primary reservoirs in the Akeyasu area. Lithologically, the Yingshan Formation is characterized by dolostones and limestones, while the Yijianfang Formation unit is predominantly composed of limestones. In terms of source rocks, mudstones and organic-rich shales within the Cambrian and Upper Ordovician strata play a major role in the Akeyasu area (Hu et al., 2016; Zhu et al., 2019). Effective reservoir spaces are created by structural fractures, pores, and dissolution caves formed during regional orogeny and karstification processes (Yun, 2008; Tian et al., 2016).

## 3. Samples and methods

Eighteen core samples, containing calcite veins, were collected from eight wells in the Yingshan and Yijianfang Formations to investigate the origin of vein-forming fluids, the timing of calcite vein generation, and fluid evolution in carbonate reservoirs within the Akeyasu area (Fig. 1 and Table 1). The analysis comprised optical and cathodoluminescence (CL) microscope observation, rare earth elements (REEs), stable isotopes of carbon ($^{13}C$), oxygen ($^{18}O$), and the $^{87}Sr/^{86}Sr$ isotopic composition. Additionally, fluid inclusion and U–Pb dating analyses were conducted on the calcite veins.

A macroscopic analysis of the core samples from the Yingshan and Yijianfang Formations was conducted to gain insight into lithology,

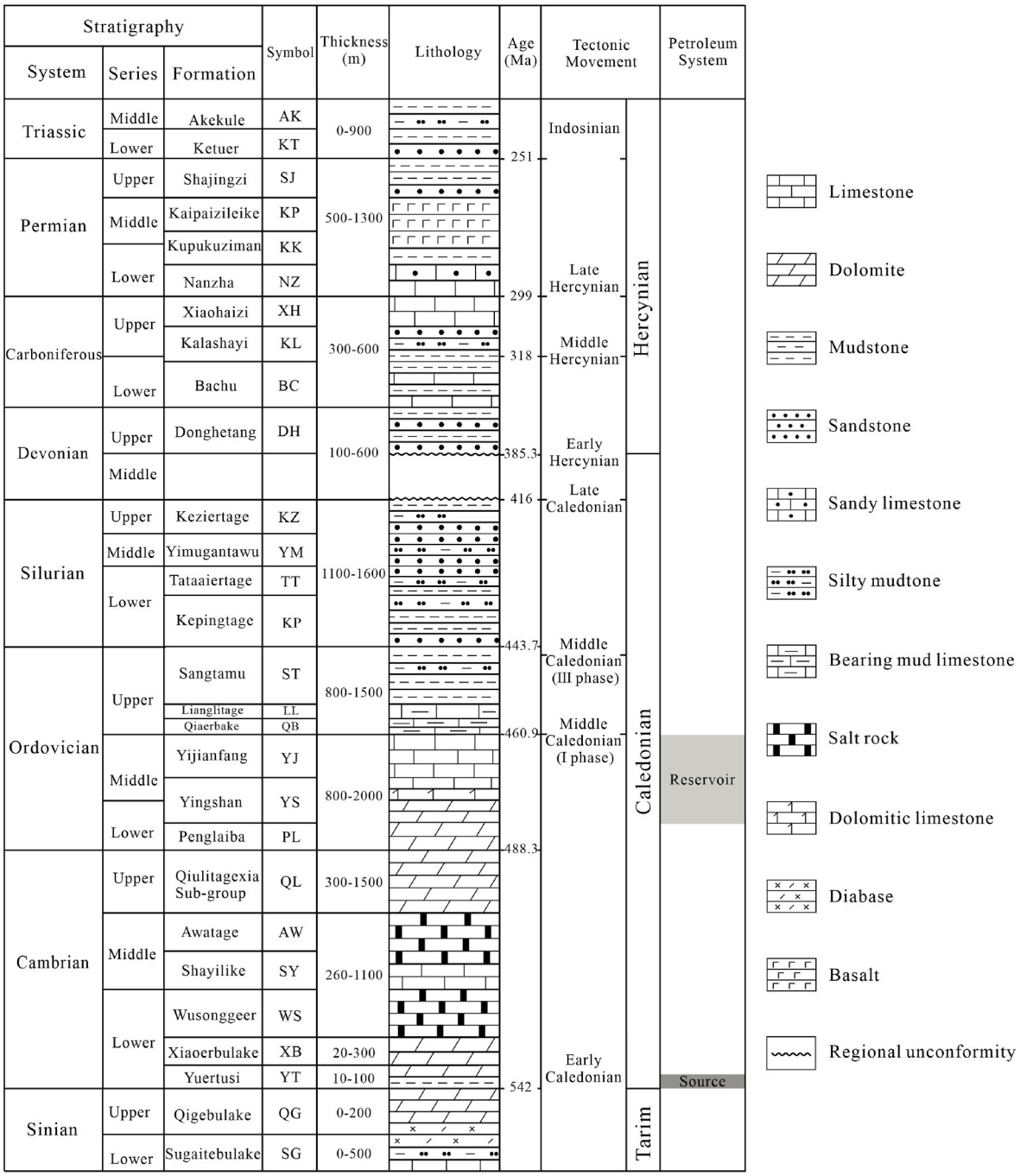


**Fig. 2.** Stratigraphic column of the Tabei Uplift, Tarim Basin, highlighting the main source rock and reservoir layers in the Akeyasu area, spanning from the Sinian to the Triassic.

color, and cross-cutting relationships of calcite veins. Subsequently, thirty-two double-sided, polished thick sections, each with a thickness of 100 μm, were prepared for microscopic petrographic observation of the calcite veins and for fluid inclusion analysis. Fluid inclusion thermometry and fluorescence analysis were performed using a NIKON-LV microscope equipped with transmitted white and incident ultraviolet (UV) sources ($\lambda$ = 365 nm). Fluorescence spectra of oil inclusions were measured with an Ocean Optics Maya 2000pro spectrometer, and quantitative fluorescence spectra parameters of $\lambda_{max}$ and QF535 (Guilhaumou et al., 1990) were used to characterize oil inclusions with varying fluorescence colors. CL imaging was conducted using a CL8200 MK5 system, running at a voltage of 10.5 kV, a current of 250 μA, and a vacuum level of 0.03 mBar to identify different types of calcite veins.

Stable carbon and oxygen isotopic analyses of the carbonates provided valuable information regarding fluid-interactions, depositional environment, and the origin of paleo-fluids (McArthur, 1994; Shields et al., 2003). Approximately 1 mg of calcite vein powder was manually micro-drilled for $^{13}C$, $^{18}O$, and $^{87}Sr/^{86}Sr$ isotopic analysis at the State Key Laboratory of Geological Processes and Mineral Resources, China University of Geosciences (Wuhan). The sampled powder was fully reacted with orthophosphoric acid at 25 °C for 24 h, and the $^{13}C$ and $^{18}O$ isotopes of $CO_2$ extracted from the reaction were determined using a Thermo Fisher MAT251EM isotope mass spectrometer, with analytical errors below 0.1‰. The Vienna Pee Dee belemnite (VPDB) standard was employed to calculate the isotope compositions. Additionally, the $^{87}Sr/^{86}Sr$ isotopic ratios of calcite veins were measured using a

**Table 1**
Sampling information, C, O and Sr isotope compositions of the carbonate samples in the Akeyasu area.

| Sample Number | Type | Well | Depth (m) | Formation | $\delta^{13}C_{VPDB}$(‰) | $\delta^{18}O_{VPDB}$(‰) | $^{87}Sr/^{86}Sr$ | Host lithology |
|---|---|---|---|---|---|---|---|---|
| S1 | C1 calcite veins | AT27X | 6915.1 | YJ | 0.1 | −12.1 | 0.709431 | Yellow-grey micrite limestone |
| S2 | C2 calcite veins | AT17 | 6416.4 | YJ | −0.8 | −7.8 | 0.708803 | Grey-black micrite limestone |
| S3 | C3 calcite veins | S118 | 5952.0 | YJ | −4.5 | −12.8 | 0.709253 | Grey-white micrite limestone |
| S4 | C3 calcite veins | S118 | 5946.3 | YJ | −2.2 | −13.0 | 0.709267 | Grey-white micrite limestone |
| S5 | C4 calcite veins | S110 | 6258.3 | YJ | −2.2 | −14.1 | 0.709711 | Grey micrite limestone |
| S6 | C4 calcite veins | AT5 | 6524.7 | YJ | −0.5 | −15.4 | 0.709748 | Yellow-grey micrite limestone |
| S7 | C1 calcite veins | AT27X | 6913.8 | YJ | −0.1 | −13.3 | 0.709417 | Limestone |
| S8 | C1 calcite veins | S110 | 6351.8 | YS | −0.3 | −12.8 | 0.709463 | Grey limestone |
| S9 | C2 calcite veins | AT21X | 6425.4 | YJ | 0.8 | −5.0 | 0.708741 | Light grey limestone |
| S10 | C2 calcite veins | AT21X | 6430.4 | YJ | 0.6 | −8.2 | 0.708701 | Grey-white micrite limestone |
| S11 | C3 calcite veins | AT36X | 5986.7 | YJ | −5.9 | −13.6 | 0.709296 | Light grey limestone |
| S12 | C3 calcite veins | AT36X | 5893.1 | YJ | −6.5 | −11.8 | 0.709132 | Grey limestone |
| S13 | C3 calcite veins | T904 | 5903.8 | YS | −4.3 | −13.0 | 0.709284 | Light grey limestone |
| S14 | C3 calcite veins | AT17 | 6417.3 | YJ | −4.3 | −13.0 | 0.709268 | Yellow-grey micrite limestone |
| S15 | C4 calcite veins | S110 | 6258.1 | YJ | −2.2 | −14.5 | 0.709716 | Limestone |
| S16 | C4 calcite veins | S110 | 6258.2 | YJ | −1.4 | −14.2 | 0.709661 | Grey micrite limestone |
| S17 | C4 calcite veins | AT5 | 6493.5 | YJ | −1.5 | −15.5 | 0.709987 | Light grey limestone |
| S18 | C4 calcite veins | AT5 | 6480.2 | YJ | −1.2 | −15.4 | 0.709646 | Yellow-grey micrite limestone |
| S1 | Host rock | AT27X | 6915.1 | YJ | −0.8 | −7.5 | 0.708814 | Yellow-grey micrite limestone |
| S2 | Host rock | AT17 | 6416.4 | YJ | −0.5 | −6.1 | 0.708962 | Grey-black micrite limestone |
| S3 | Host rock | S118 | 5952.0 | YJ | −1.0 | −7.2 | 0.708800 | Grey-white micrite limestone |
| S5 | Host rock | S110 | 6351.8 | YS | 0.1 | −8.6 | 0.708881 | Grey micrite limestone |

Nu-Instrument high-resolution MC-ICP-MS, with mass fractionation corrected by $^{86}Sr/^{88}Sr = 0.1194$. The mean $^{87}Sr/^{86}Sr$ ratios of the international standard sample SRM-987 were determined to be 0.710249 ± 0.000003 (2σ, N = 7), with this sample serving as a drift monitor. The precision of the $^{87}Sr/^{86}Sr$ isotopic analysis was better than 0.004%.

Laser ablation–inductively coupled plasma–mass spectrometry (LA-ICP-MS) was employed for in-situ U–Pb dating of calcite veins at the Radiogenic Isotope Facility, University of Queensland, following standard procedures. Initial scans of the samples were performed using the RESOlution SE laser ablation system and the Thermo iCap-RQ quadrupole ICPMS to assess their $^{206}Pb$, $^{207}Pb$, $^{208}Pb$, and $^{238}U$ ion beam content. Subsequently, samples showing high U/Pb ratios and low common Pb contents were selected for in situ U–Pb dating of calcite via LA-ICP-MS. The laser ablation spot diameter used was 100 μm, with a laser repetition rate of 10 Hz and energy density of 2.5 J/cm$^2$. Helium served as the primary carrier gas during laser ablation, while argon and nitrogen were introduced to enhance signal intensity. Each laser ablation spot sequence comprised a 20-s pre-ablation background, followed by a 25-s ablation of the target spot and a subsequent 10-s washout. A 2-s pre-ablation was conducted on each spot before analysis to remove any surface contamination. Regular testing with the NIST612 glass standard for normalization and 43Ca as an internal standard was performed, while NIST614 glass standard was used to correct for the $^{207}Pb/^{206}Pb$ fractionation, ensuring instrument accuracy. Additionally, the AHX-1a standard sample, with a U–Pb age of 209.8 Ma, was employed to correct the $^{238}U/^{206}Pb$ ratios, as previously described (Liu et al., 2021). Raw data underwent processing using Iolite 3.71, a software developed by the University of Melbourne, Australia, and ages were determined from Tera-Wasserburg lower intercepts using Isoplot 3.75 software. Ages are reported at 2σ confidence intervals, accounting for both systematic and analytical uncertainties.

In-situ rare earth elements (REEs) analysis of calcite veins by LA-ICP-MS was conducted at the Sample-Solution Analytical Technology Co. Ltd. In Wuhan, China, following established methods described by Zong et al. (2017). REEs were categorized into light rare earth elements (LREE), medium rare earth elements (MREE), and heavy rare earth elements (HREE). To assess REE enrichment, ratios after normalization were employed. Specifically, $Pr_N/Tb_N$ ratios was substituted for $LREE_N/MREE_N$, $Pr_N/Yb_N$ ratios for $LREE_N/HREE_N$, and $Tb_N/Yb_N$ ratios for $MREE_N/HREE_N$, following Lawrence et al. (2006). In this study, the Post-Archaean Australian Shale Standard (PAAS) was used for normalizing the REE + Y elemental compositions of both calcite veins and host rocks (Taylor and McLennan, 1985). In addition, the Ce anomalies was analyzed by using the $(Ce/Ce^*)_N$ versus $(Pr/Pr^*)_N$ plot to eliminate the interference caused by possibly anomalous abundances of La (Bau and Dulski, 1996).

## 4. Results

### 4.1. Petrography of calcite veins

The petrographic examination of core samples reveals the widespread occurrence of calcite veins within the specimens investigated (see Fig. 3). We have identified two distinct types of calcite vein textures within these core samples, as illustrated in Fig. 3: pore or vug-filling calcite veins (Fig. 3A and F) and fracture-filling calcite veins (Fig. 3B–E). Pore-filling calcite veins are often seen as cementitious materials filling the voids created by dissolved particles. On the other hand, fracture-filling calcite veins are primarily observed within high-angle fractures, where calcite has precipitated to occupy these fracture spaces. Notably, vug-filling calcite veins are predominantly characterized by coarse crystalline calcite grains and are primarily found within the larger karst caves within the Ordovician reservoirs. No obvious cross-cutting relationships of calcite veins were observed in the core samples. Four phases of calcite veins (C1–C4) were identified based on detailed petrographic and geochemical data including REE distribution patterns, $\delta^{13}C$, $\delta^{18}O$, $^{87}Sr/^{86}Sr$ isotopic ratios. In the study area, calcite veins mostly exhibit dull brown CL colors but rarely display bright orange CL colors. Three types of CL colors of calcite veins were observed (Fig. 4), indicating multiple stages of fluid flow events in the Yingshan and Yijianfang Formations reservoir intervals. The C1 calcite veins with fine crystals are mainly filled in the dissolution pores, and do not emit light under cathode ray irradiation (Fig. 4 B). The C2 and C3 calcite veins are developed along high-angle fractures with a dark brown color under CL (Fig. 4 D and 4 F). Most of the vugs are filled with the C4 calcite veins which have bright-orange color under CL (Fig. 4 H).

### 4.2. Rare-earth elements + yttrium (REE + Y) elements of calcite veins

The REE + Y content and distribution patterns of the calcite veins are shown in Figs. 5 and 6. PAAS-normalized plot shows coherent REE + Y distribution patterns. All the calcite veins and host rocks in the study area are characterized by slight enrichment of middle REE compared to light REE and heavy REE, except for the C1 calcite veins which display a

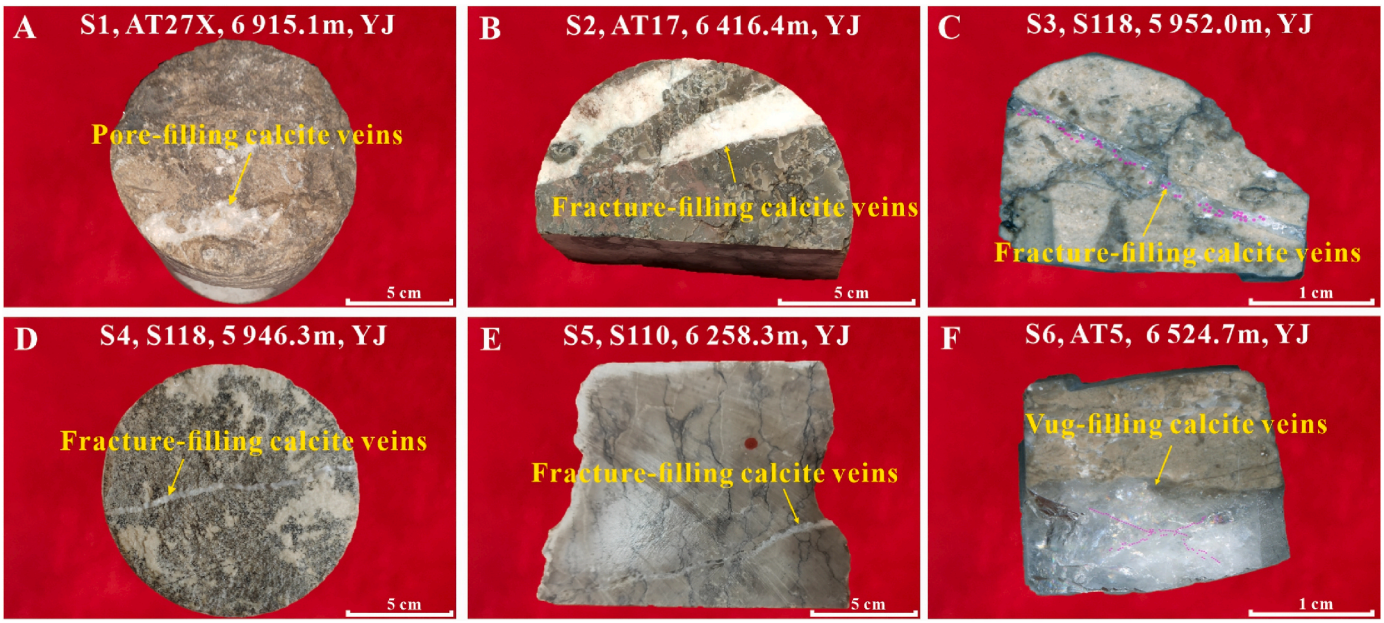


**Fig. 3.** Images of the two representative calcite vein textures in the deep-burial Ordovician carbonate reservoirs of the Akeyasu area. A: Yellow-grey micrite limestone filled with pore-filling calcite veins; B: Grey micrite limestone with fracture-filling calcite veins; (C–E) Grey-white micrite limestone with fracture-filling calcite veins; (F) Grey limestone with vug-filling calcite veins.

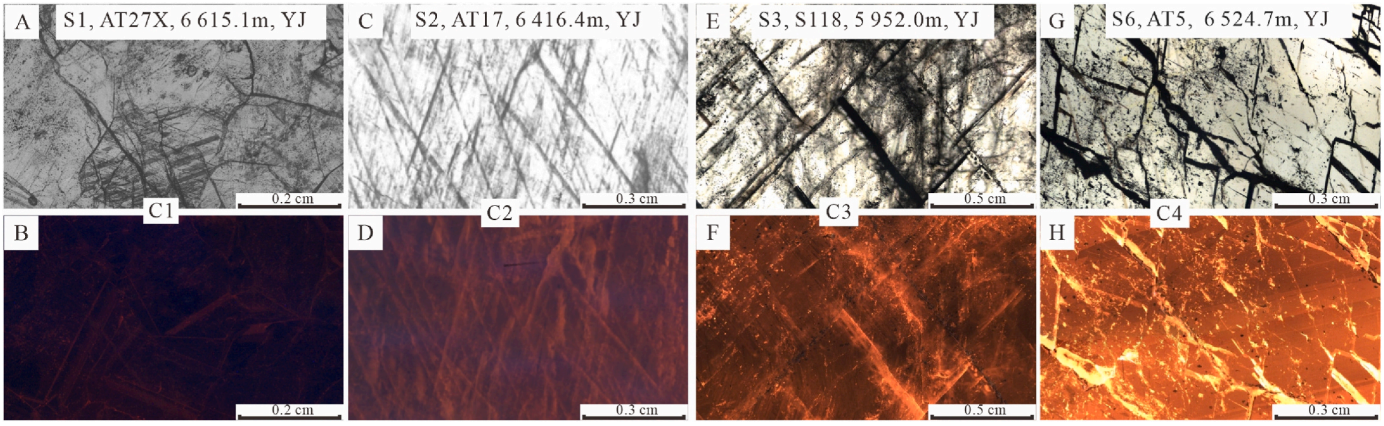


**Fig. 4.** Photomicrographs of calcite veins under transmitted light and cathodoluminescence. A–B: C1 calcite veins characterized by not emitting light under cathode ray irradiation. B–F: Transmitted light and cathodoluminescence photomicrographs show that C2 and C3 calcite veins have a uniformly dark-brown color under cathodoluminescence. G–H: C4 calcite veins' micrographs under transmitted light and cathodoluminescence, with C4 calcite having a bright-orange color under cathodoluminescence.

relatively uniform feature (Fig. 5).

The PAAS-normalized REE + Y patterns of the C1 calcite veins are relatively flattened. The total rare earth element contents (ΣREE) values are ranged from 1.63p pm to 3.33 ppm, with an average value of 2.29 ppm (Fig. 5A). The C2 and C3 calcite veins have a similar REE + Y distribution pattern with those of host rocks, which display obvious depletions of light REE and positive Yttrium (Y) anomalies (Fig. 5B and C). Compared with C2 calcite veins and host rocks, C3 calcite veins show obvious negative Ce anomalies and relatively high Y/Ho ratio (Fig. 6). The 'negative' Ce anomalies shows in the REE + Y patterns of the C2 calcite veins and the host rocks are caused by anomalous abundances of La (Bau and Dulski, 1996). The ΣREE values of C2, C3 calcite veins and host rocks range from 12.94 ppm to 17.44 ppm, 7.71 ppm–14.83 ppm and 13.32 ppm–14.76 ppm, respectively. The calculated δCe values of the C3 calcite veins vary from 0.61 to 0.70, with average values of 0.66, respectively. There are also insignificant Eu anomalies in the C2 and C3 calcite veins, with the δEu values ranging from 0.98 to 1.11. The PAAS-normalized REE + Y patterns of the C4 calcite veins display weak negative Eu anomalies, weak positive Y anomalies, and obvious enrichment in MREE (Fig. 5D), which are characterized by $Pr_N/Tb_N < 1$ and $Tb_N/Yb_N > 1$. The ΣREE values of the C4 calcite veins are relatively higher than the C1, C2 and C3 calcite veins, ranging from 20.66 ppm to 63.74 ppm, with an average value of 49.16 ppm. The δEu values of the C4 calcite veins range from 0.82 to 0.90, with an average value of 0.85. However, δCe values of the C4 calcite veins range from 0.98 to 1.06, with an average value of 1.02, which shows no obvious anomalies.

### 4.3. C, O isotopic ratios

The $\delta^{13}C$ and $\delta^{18}O$ values of calcite vein and host rock samples in the study area are shown in Table 1. Calcite vein samples exhibit large variations in $\delta^{13}C$ and $\delta^{18}O$ values (Figs. 7 and 8). The host rocks have $\delta^{13}C$ and $\delta^{18}O$ range values from 0.19‰ to −0.10‰ and −8.59‰ to −6.10‰, which are consistent with the results in previous studies from

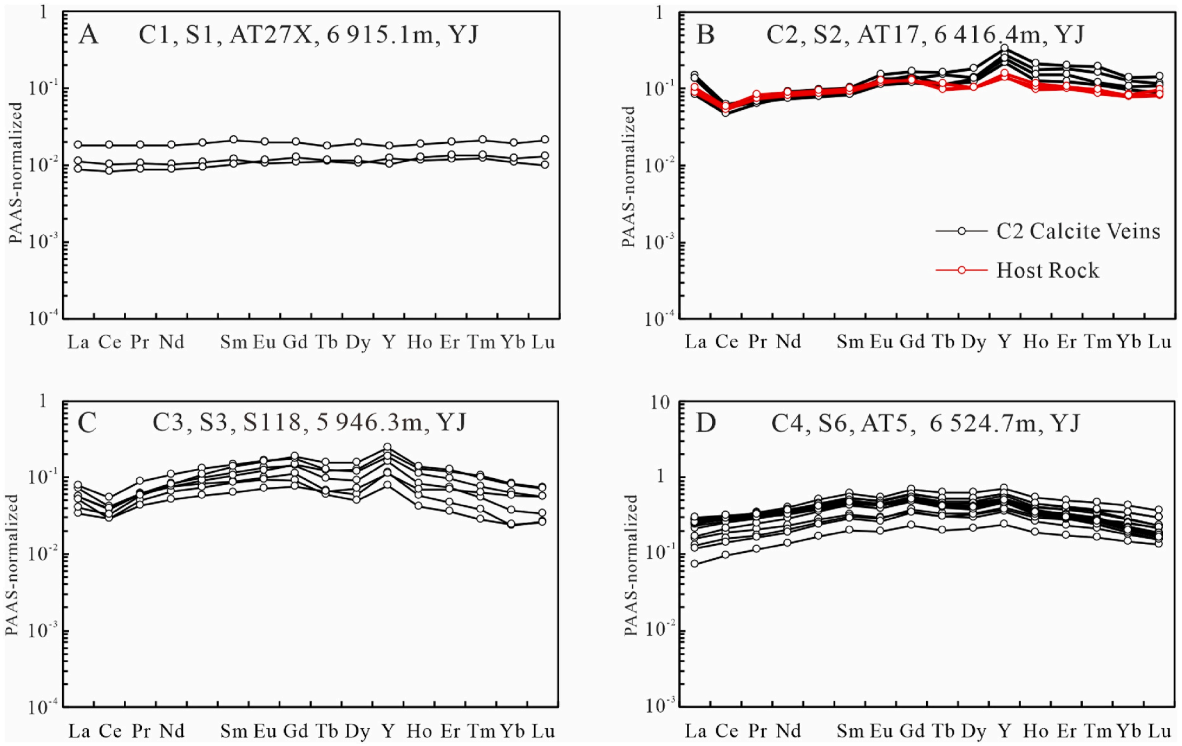


**Fig. 5.** Plot of PAAS-normalized REE + Y patterns of the calcite veins from the deep burial Ordovician carbonate reservoirs of the Akeaysu area showing the difference in REE + Y distribution patterns of C1, C2, C3, C4 calcite veins and host rock. A: A relatively flattened REE + Y distribution pattern of the C1 calcite veins. B–C: The C2 and C3 calcite veins have a similar REE + Y distribution pattern with the host rock, which shows abundant HREE enrichment with positive Y and negative Ce anomalies. D: The C4 calcite veins have high HREE enrichment, displaying positive Y and weak negative Eu anomalies REE + Y distribution pattern.

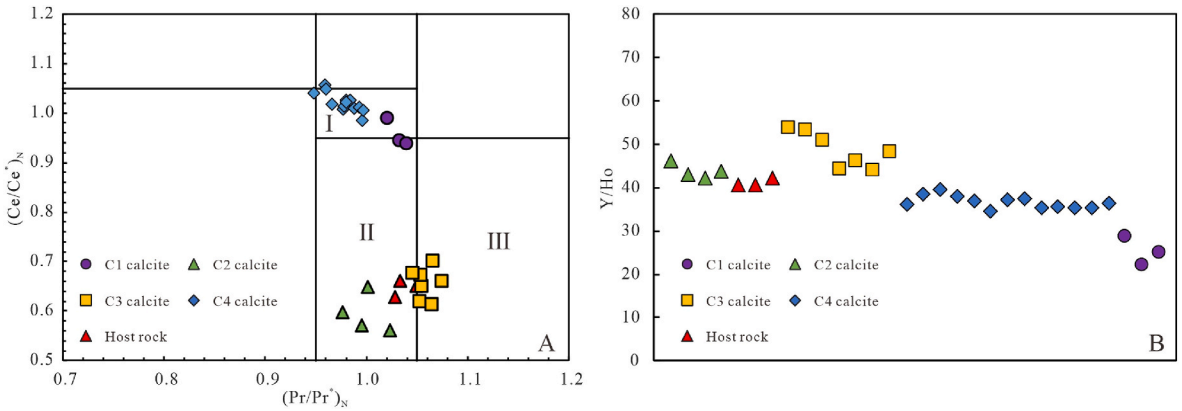


**Fig. 6.** A: Calcite veins from deep burial Ordovician carbonate reservoirs of the Akeaysu area in a graph of $(Ce/Ce^*)_N$ versus $(Pr/Pr^*)_N$. Field II: neither $Ce_N$ nor $La_N$ anomaly; field II: Positive $La_N$ anomaly, no $Ce_N$ anomaly; field III: negative $Ce_N$ anomaly. B: Scatterplot showing the Y/Ho ratios of calcite vein and host rock samples from the deep burial Ordovician carbonate reservoirs in the Akeyasu area.

this region (Liu et al., 2008; Han et al., 2019). $\delta^{13}C_{VPDB}$ values of C1, C2 and C4 calcite veins vary from −0.09‰ to +0.10‰, −0.84‰ to +0.81‰ and −2.20‰ to −0.50‰ respectively. $\delta^{13}C$ values for C3 calcite veins range from −6.50‰ to −2.15‰, which are lower than those of host rocks (Fig. 7). The C2 calcite veins have similar $\delta^{18}O$ values with the host rocks, ranging from −8.19‰ to −7.40‰. $\delta^{18}O_{VPDB}$ values for C1, C3 and C4 calcite veins range from −13.79‰ to −12.1‰, −13.59‰ to −11.80‰ and −15.51‰ to −14.10‰, respectively.

### 4.4. Sr isotopic ratio

The $^{87}Sr/^{86}Sr$ ratios of calcite veins in the study area vary from 0.708701 to 0.709746 (Table 1). $^{87}Sr/^{86}Sr$ values of C2 calcite veins and host rocks fall in the similar range recorded for the Early-Middle Ordovician seawater (Fig. 8; McArthur et al., 2001; Huang et al., 2004), with values from 0.708701 to 0.708803. The $^{87}Sr/^{86}Sr$ values for C1, C3 and C4 calcite veins range from 0.709417 to 0.709463, 0.709132 to 0.709296 and 0.709646 to 0.709987, respectively, which are higher than the $^{87}Sr/^{86}Sr$ values of the Early-Middle Ordovician seawater (Fig. 8).

### 4.5. U–Pb isotopic ages of calcite veins

The LA-ICP-MS *in-situ* U–Pb isotopic analysis was conducted for six typical calcite vein samples from the study area. All analyzed calcite veins show relatively low common Pb contents, variable concentrations

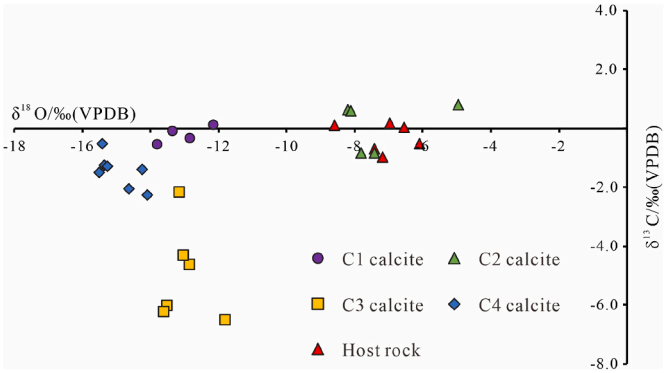


**Fig. 7.** Cross plot of $\delta^{13}C$ versus $\delta^{18}O$ for sampled calcite veins and host rocks from the deep burial Ordovician carbonate reservoirs in the Akeyasu area.

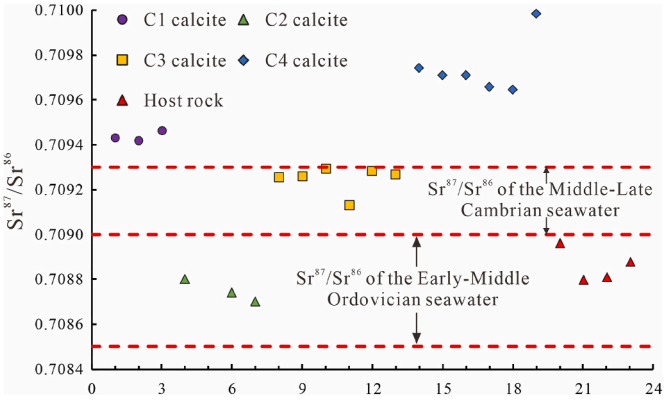


**Fig. 8.** Scatterplot showing the $^{87}Sr/^{86}Sr$ values of calcite vein and host rock samples from the deep burial Ordovician carbonate reservoirs in the Akeyasu area. The $^{87}Sr/^{86}Sr$ ratios for the Early-Middle Ordovician seawater (Huang et al., 2004) are highlighted.

of U and a wide range of U/Pb ratios ($0.44 \leq {}^{238}U/^{206}Pb \leq 27.51$), which defined high-precision U–Pb calcite ages with 2σ errors better than 4% (Fig. 9). A total of sixty-two analytical spots in the C1 calcite veins indicate that $^{238}U/^{206}Pb$ and $^{207}Pb/^{206}Pb$ ratios range from 0.12 to 14.07 and 0.06 to 0.89. Integrated with Tera-Wasserburg Concordia diagrams, the result in lower intercept age for C1 calcite veins is 459.8 ± 4.7 Ma, with mean squared weighted deviates (MSWD) of 1.6 (Fig. 9A). Eighty-three in situ spot analyses for the C2 calcite veins exhibit a wide range of $^{238}U/^{206}Pb$ ratios (6.14–15.33) and give an isochron on the Tera-Wasserburg Concordia diagrams corresponding to a lower intercept age of 418.8 ± 3.7 Ma (MSWD = 1.5) (Fig. 9B). For the C3 calcite veins, sample 3 (n = 105) and sample 4 (n = 87) have U contents range from 0.213 ppm to 1.864 ppm, 0.009 ppm to 0.241 ppm and Pb contents range from 0.001 ppm to 0.136 ppm and 0.001 ppm to 0.081 ppm, with corresponding $^{238}U/^{206}Pb$ ratios vary from 9.95 to 19.28, 1.16 to 21.10 and 0.05 to 0.77, respectively. These U–Pb isotopic data yield two isochron ages at 329.7 ± 1.6 Ma and 310.0 ± 3.6 Ma, with the MSWD of 1.14 and 1.3 (Fig. 9C and D). The sample 5 (n = 42) and sample 6 (n = 72) for the C4 calcite veins have $^{238}U/^{206}Pb$ and $^{207}Pb/^{206}Pb$ ratios vary from 7.62 to 22.82, 2.90 to 20.54 and 0.02 to 0.69, 0.27 to 0.74, respectively. When plotted on Tera-Wasserburg diagrams, the lower intercept ages for sample 5 and sample 6 are 291.7 ± 6.1 Ma and 220.5 ± 7.3 Ma, with the MSWD of 4.3 and 2.0 (Fig. 9E and F).

### 4.6. Fluid inclusion petrography

In the study area, a variety of hydrocarbon inclusions were identified, including single-phase liquid inclusions, two-phase gas-liquid inclusions, and three-phase gas-liquid-solid bitumen-bearing inclusions. The two-phase gas-liquid inclusions are particularly noteworthy, showing small gas bubbles at room temperature. These inclusions display elliptical, slender, and irregular shapes, with diameters spanning from 2 μm to 15 μm. Our investigation revealed that the oil inclusions in this study area are predominantly secondary inclusions, often situated along healed micro-fractures within the calcite veins. A smaller quantity of primary oil inclusions was also observed, distributed either randomly or arranged along growth bands in single crystals or as isolated inclusions within the calcite veins. Representative micrographs depicting primary oil inclusions are provided in Fig. 10. Within the study area, three distinct types of primary oil inclusions were detected based on their microscopic fluorescence characteristics and measured fluorescence spectra. In the C1 calcite veins, primary oil inclusions showed a golden yellow fluorescence, with $\lambda_{max}$ values of the fluorescence spectrum ranging from 560 nm to 568 nm (Fig. 10A–D). In the C3 calcite veins, primary oil inclusions displayed yellow fluorescence, with $\lambda_{max}$ values ranging from 530 nm to 536 nm (Fig. 10E–H). Finally, the C4 calcite veins predominantly contained primary oil inclusions with yellow white to yellow-green fluorescence, featuring $\lambda_{max}$ values of 500~516 nm (Fig. 10I-L). It is noteworthy that no primary oil inclusions were detected in the C2 calcite veins within the scope of this study.

## 5. Discussion

### 5.1. Origin of vein-forming fluids

To gain insights into the properties, origins, redox environments, and temperature of diagenetic fluids, we use the REEs systematics, $\delta^{13}C$, $\delta^{18}O$, and $^{87}Sr/^{86}Sr$ isotopic ratios of these calcite veins. The REE + Y distribution patterns, $\delta^{13}C$, $\delta^{18}O$, and $^{87}Sr/^{86}Sr$ values for the host rocks align with those characteristics of Early-Middle Ordovician seawater (Figs. 6 and 7), corroborating that post-depositional processes have had minimal impact on the host rocks (Veizer et al., 1999; Van Kranendonk et al., 2003; Liu et al., 2008).

The C1 calcite veins, predominantly occupying dissolution pores (Fig. 3 A), show flattened REE + Y distribution patterns (Fig. 5A) and lower ΣREE concentrations. The depletion of $^{18}O$ and lower Y/Ho ratios (22.0–28.6) for the C1 calcite veins may point to a meteoric water source. The REE + Y distribution pattern of marine carbonate rocks can be flattened by mixing with a small amount of silicate minerals through fluid-rock interaction (Van Kranendonk et al., 2003). A reasonable explanation for the obvious $^{18}O$-depletion is that the oxygen isotope is more sensitive to diagenesis and simpler to exchange isotopes with diagenetic fluids as the carbon volume in carbonate rocks is significantly greater than that in diagenetic fluids (Banner and Hanson, 1990). The lower concentrations of REEs could relate to the limited solubility of REE + Y in meteoric water at ambient temperature (Zhao et al., 2019).

Distinguishing between C2 and C3 calcite veins is facilitated by their distinct REE + Y compositions, $\delta^{13}C$, $\delta^{18}O$, and $^{87}Sr/^{86}Sr$ isotopic characteristics and U–Pb isotopic ages, despite their similar dark-brown CL colors, ΣREE values, and REE + Y distribution patterns (Fig. 4 C–F and Fig. 5B–C). U–Pb isotopic age data for C2 and C3 calcite veins cluster around two distinct groups, showing two phases of calcite vein precipitation (Fig. 9B–D). The resemblance in $\delta^{13}C$, $\delta^{18}O$, $^{87}Sr/^{86}Sr$, ΣREE values, and REE + Y distribution patterns between C2 calcite veins and host rocks (Figs. 6 and 7; Table 1) suggests that C2 calcite veins have a local fluid source, primarily originating from Early-Middle Ordovician formation water.

In contrast, C3 calcite veins display higher $^{87}Sr/^{86}Sr$ ratios than both C2 calcite veins and host rocks (Fig. 8), implying an external fluid contribution with elevated $^{87}Sr/^{86}Sr$ levels. This is consistent with the stability of strontium isotopic compositions in open seawater throughout geological periods (Palmer and Elderfield, 1985; McArthur et al., 1992; Banner, 2004). The $^{87}Sr/^{86}Sr$ ratios of C3 calcite veins align

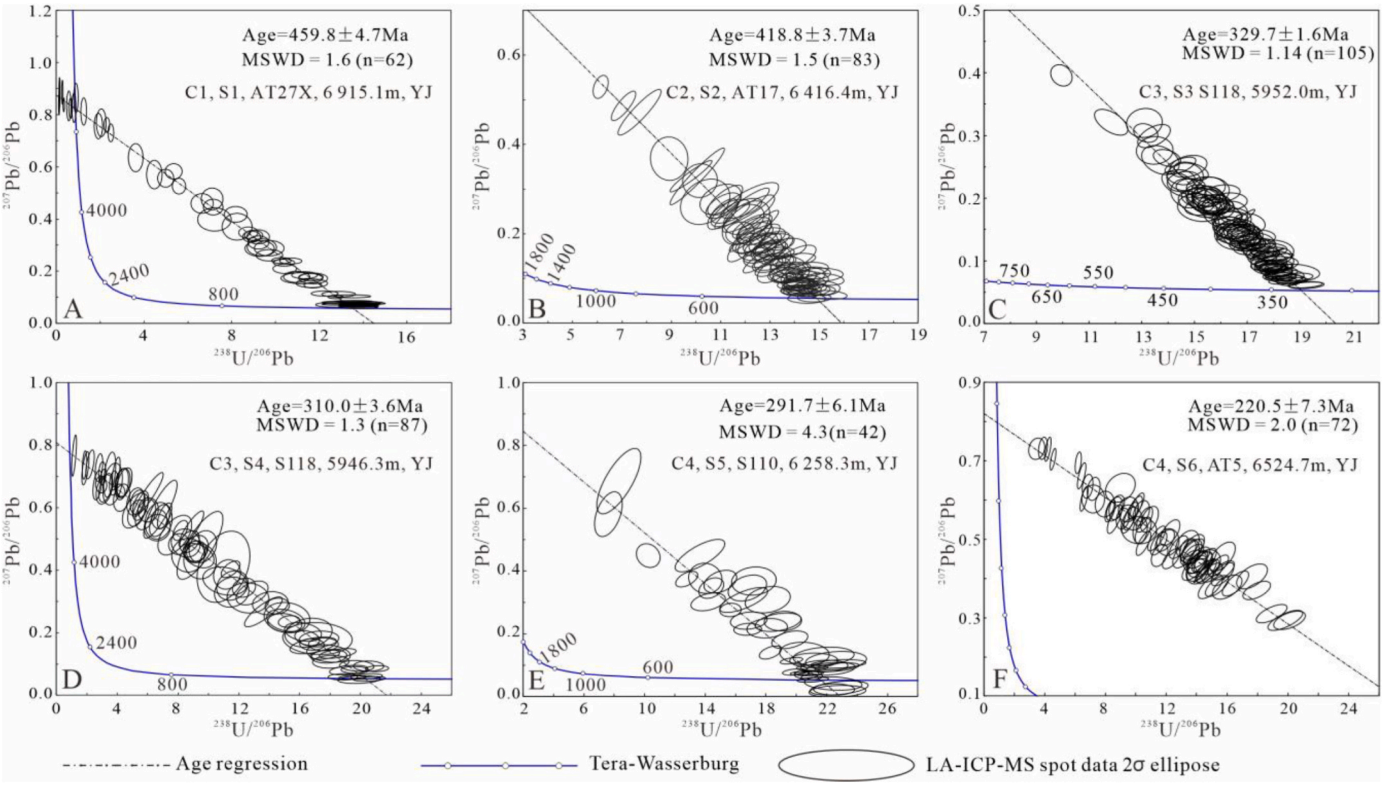


**Fig. 9.** Tera-Wasserburg concordia plots showing U–Pb dating of C1, C2, C3, and C4 calcite veins from the deep-burial Ordovician carbonate reservoirs of the Akeyasu area. Samples are arranged from oldest to youngest, top left to bottom right. A: C1 calcite veins sampled from well AT27X (6915.1m) yield a U–Pb age of 459.8 ± 4.7Ma with a MSWD of 1.6. B: C2 calcite veins sampled from well AT17 (6416.4m) define a lower intercept U–Pb age of 418.8 ± 3.7Ma with a MSWD of 1.5. C–D: U–Pb dating suggests C3 calcite veins (sampled from well S118, 5952.0m and 5946.3) precipitation occurred at 329.7 ± 1.6Ma and 310.0 ± 3.6Ma. D–E: The age of C4 calcite veins (sampled from well S110, 6258.3m and well AT5, 6524.7m) revealed by U–Pb dating are 291.7 ± 6.1Ma and 220.5 ± 7.3Ma.

with those of Middle-Late Cambrian seawater (Fig. 8). The prominent negative Ce anomalies, positive Y anomalies, and weak positive Gd anomalies represent a typical REE + Y distribution pattern for marine carbonate rocks (German and Elderfield, 1989; Alibert and McCulloch, 1993). Thus, we hypothesize that the fluids responsible for C3 calcite vein formation originated from Middle-Late Cambrian formation water. The $^{13}C$-depletion observed may be attributed to the incorporation of organic carbon, as two distinct local carbon pools with substantially negative $\delta^{13}C$ values are commonly found in most carbonates: carbonate fractions in adjacent host rocks and organic matter (Hooker et al., 2017).

Distinctive features of C4 calcite veins include their bright-orange CL colors (Fig. 4G–H), weak negative Eu anomalies, a slight enrichment of Middle Rare Earth Elements (MREE) in PAAS-normalized REE + Y distribution patterns, and higher REEs contents (Fig. 5D). Furthermore, C4 calcite veins exhibit notably lower $\delta^{18}O_{VPDB}$ values (Fig. 7) and higher $^{87}Sr/^{86}Sr$ ratios (Fig. 8) compared to C1, C2, C3 calcite veins, and host rocks. The enrichment of MREE and weak negative Eu anomalies suggest that C4 calcite veins originated from low-temperature hydrothermal fluids (Alexander et al., 2008; Johannessen et al., 2017; Chen et al., 2022a). The weak negative Eu anomalies may result from fractional crystallization of plagioclase in intermediate-acidic magmatic rocks, such as rhyolites or dacite (Tian et al., 2010). In addition, fluorite was observed in C4 calcite veins (Fig. 11). Although the presence of fluorite may be related to hydrocarbon migration (Caja et al., 2006), the fluorite reported in the Ordovician reservoirs in the Tarim Basin is mainly of hydrothermal origin (Wang et al., 2014; Jia et al., 2022). Increased hydrothermal temperature increases thermodynamic fractionation, resulting in lower $\delta^{18}O_{VPDB}$ values of C4 calcite veins. The highest $^{87}Sr/^{86}Sr$ ratios may be attributed to the mixing of Cambrian clastic rocks during the vertical upward migration of hydrothermal fluids via the fault system (Jin et al., 2013).

### 5.2. Relationship between the tectonics and fluid flow

The presence of primary oil inclusions within the calcite veins provides strong evidence that oil charging coincided with calcite precipitation, as previously reported (Chen et al., 2022a; Cong et al., 2022). These primary oil inclusions, observed in calcite veins from the deep-burial Ordovician reservoirs of the Akeyasu area, exhibit a random distribution or are arranged along growth bands within individual calcite crystals (Fig. 10). Similar observations of primary oil inclusions have also been made in the Halahatang Oilfield, Tabei Uplift (Cong et al., 2022). In our study, we have identified three types of primary oil inclusions within calcite veins from the Yingshan and Yijianfang Formations (Figs. 10 and 11). These findings suggest the occurrence of three separate oil charging events in the Ordovician reservoirs. It is important to note that the oil discovered in the deep-burial Ordovician carbonate reservoirs of the Akeyasu area belongs to a single genetic group and primarily originates from the marine shale of the Lower Cambrian Yuertusi Formation (Zhang and Huang, 2005; Hanson et al., 2000).

The primary oil inclusions exhibit distinct fluorescence colors, including golden yellow (Fig. 10A–D), yellow (Fig. 10E–H), and yellow green (or yellow white) (Fig. 10I-L). These differences in fluorescence are associated with varying $\lambda_{max}$ values, ranging from 560 nm to 568 nm, 530 nm–536 nm, and 500 nm–516 nm, respectively. The $Q_{650/500}$ values for these primary oil inclusions range from 0.80 to 1.00, 0.26 to 0.55, and 0.26 to 0.40 (Fig. 12). Decreasing $Q_{650/500}$ values and increasing $\lambda_{max}$ values in the golden yellow, yellow, and yellow green (or yellow white) inclusions show increasing maturity levels of the enclosed oils (Hagemann and Hollerbach, 1986; Ping et al., 2020).

Cross-section GG' reveals the presence of four distinct fault groups within the Paleozoic strata of the Akeyasu area (Fig. 13). Certain subvertical segments of multi-stage active faults originate from the top of

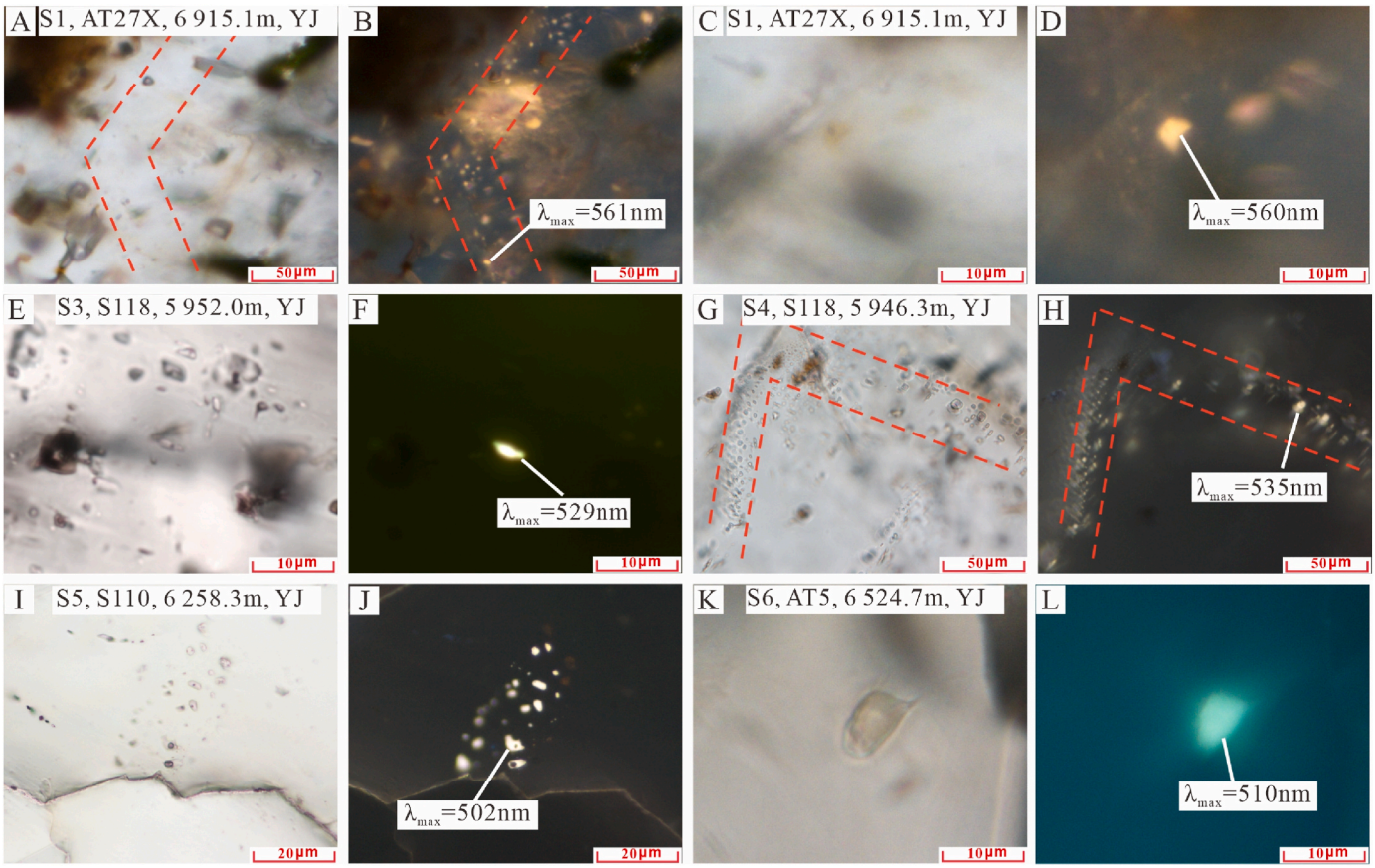


**Fig. 10.** Photomicrographs of oil inclusions in C1, C3 and C4 calcite veins. A–B: Primary oil inclusions with golden yellow fluorescence colors are arranged along a growth band in the C1 calcite veins. C–D: Primary oil inclusions with golden yellow fluorescence colors are isolated in the C1 calcite veins. E–F: Isolated primary oil inclusions with yellow fluorescence colors in the C3 calcite veins. G–H: Primary oil inclusions with yellow fluorescence colors are distributed along growth zones of the host C3 calcite. I–J: Primary oil inclusions with yellow-white fluorescence colors are randomly distributed in C4 calcite veins. K–L: Isolated primary oil inclusions with yellow-green fluorescence colors in the C4 calcite veins.

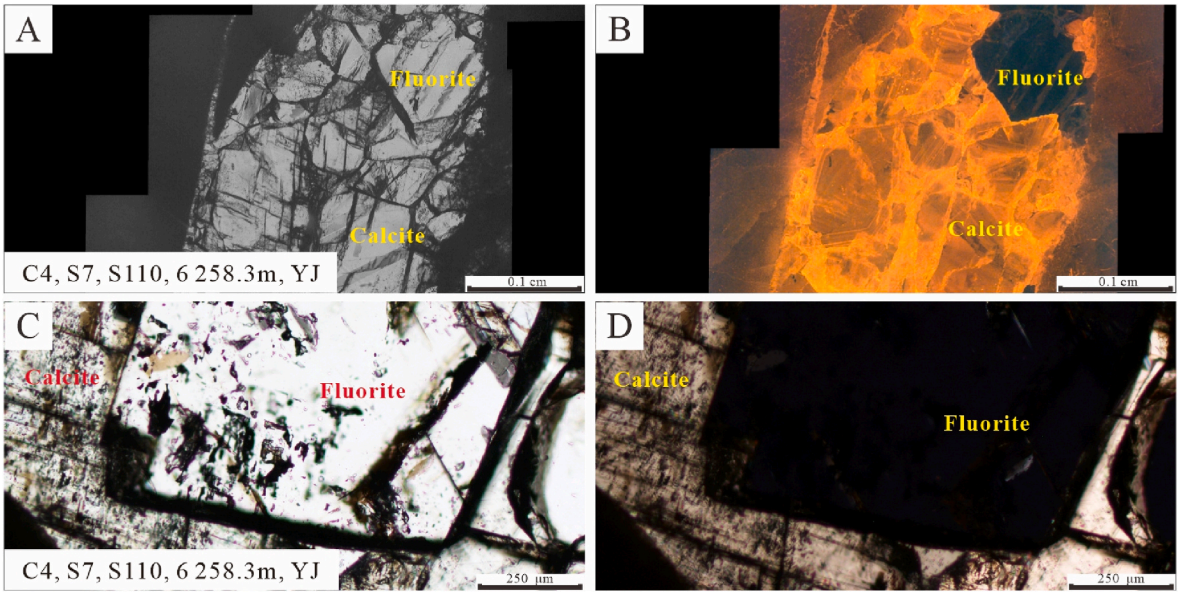


**Fig. 11.** Photomicrographs showing petrographic characteristics of fluorite in the C4 calcite veins. A–B: Images of fluorite under transmitted light and cathodoluminescence. Fluorite is characterized by the negative low protrusion under transmitted light and having a dark purple color under cathodoluminescence. C–D: Photomicrographs of fluorite under transmitted light and crossed-polarized light, showing complete extinction under crossed polarized light.

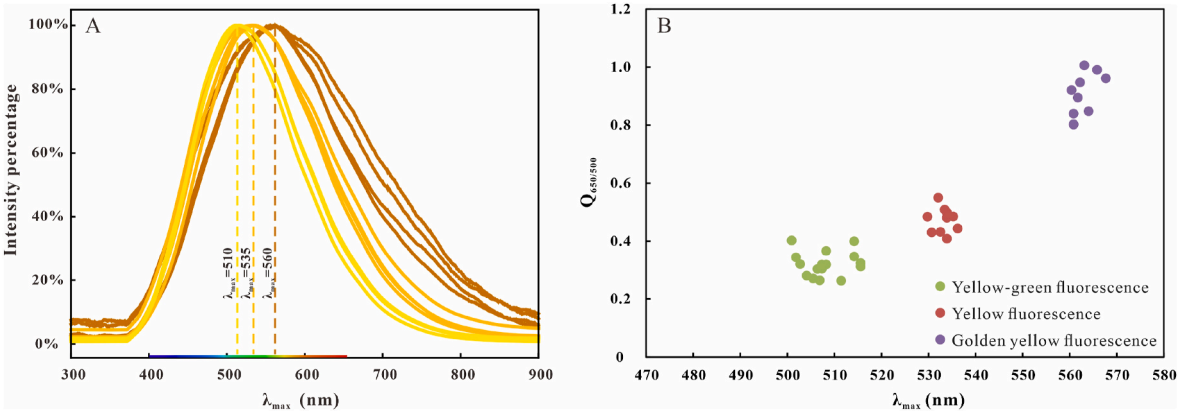


**Fig. 12.** A: Plot of measured fluorescence spectra of oil inclusions in C1, C3 and C4 calcite veins from the deep Ordovician carbonate reservoirs of the Akeyasu area; (B): Relationship between the fluorescence spectra parameters $\lambda_{max}$ and $Q_{650/500}$ of oil inclusions in C1, C3 and C4 calcite veins from the deep Ordovician carbonate reservoirs of the Akeyasu area.

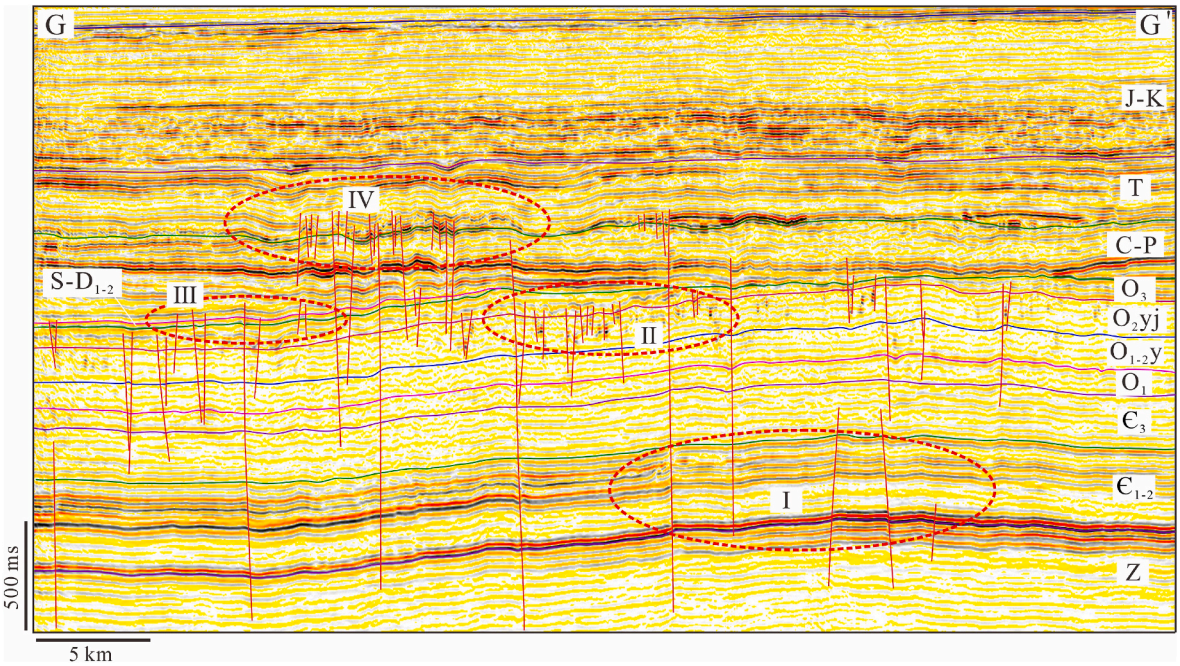


**Fig. 13.** A representative seismic section showing faults developed and interpreted structural activation phases in the Akeyasu area. Four phases of tectonic phases and fault groups were identified in the Akeyasu area as follows: I) faults formed during the Early Caledonian orogeny; II) faults developed during the Middle Caledonian orogeny; III) faults that developed during the Late Caledonian-Early Hercynian orogeny; IV) faults formed during the Middle-Late Hercynian orogeny. The location of the cross-section GG' is marked in Fig. 1C.

the Sinian and extend upward through the top of the Middle Ordovician. Seismic data show that most strike-slip faults are confined between the bottom of the Late Cambrian and the top of the Middle Ordovician (Fig. 13). These Paleozoic faults are characterized by steep dips and exhibit flower-like or Y-shaped features (Fig. 13). Except for normal faults that cut through Early Cambrian layers, faults within the Paleozoic strata are predominantly reverse faults (Fig. 13). The interpretation of fault patterns and the stratigraphic horizons intersected by faulting can provide insights into the timing and duration of fault activities (Tao et al., 2022; He et al., 2022). Group-I faults reflect faulting during the Early Caledonian Orogeny, primarily characterized by normal faults resulting from extensional stress (Shi, 2020; Wu et al., 2021). Some of these normal faults were later reactivated and reversed during the Middle Caledonian Orogeny, forming reverse faults. Group-II faults are associated with the Middle Caledonian Orogeny, marked by a transition from extension to compression (Deng et al., 2022). These faults consist mainly of high-angle reverse faults cutting the Middle-Lower Ordovician strata and are represented as north-northeast trending strike-slip faults on the top of the Middle Ordovician (Fig. 1C). Group-III faults record fault activity during the Late Caledonian-Early Hercynian Orogeny and predominantly involve the reactivation of Group-II faults (Deng et al., 2022). Intense compression during this phase led to the reactivation of high-angle reverse faults, primarily within the Lower-Middle Devonian strata. Prolonged denudation in the region resulted in the formation of two regional unconformities between the Silurian and Devonian (Fig. 2). Group-IV faults represent significant faulting during the Middle-Late Hercynian Orogeny (Wu et al., 2021; Yang et al., 2022a). Deep strike-slip faults were reactivated, leading to the formation of a series of reverse faults in overlying strata. These fault segments extend upward into the Upper-Triassic strata. Additionally, a northeast trending strike-slip fault formed during this tectonic phase (Fig. 1C).

The Ordovician reservoirs in the Akeyasu area underwent multi-

stages of fluid activities and formed four phases of calcite veins. Calcite veins with distinct REE + Y compositions, $\delta^{13}C$, $\delta^{18}O$, and $^{87}Sr/^{86}Sr$ isotopic characteristics were formed during each tectonic period. Based on the analysis of phases of calcite veins, origin of vein-forming fluids and tectonics, the relationship between the tectonics and fluid flow in the Akeyasu area can be summarized as follows (Fig. 14):

The C1 calcite veins are suggested to precipitate from meteoric water during the tectonic uplifts, which are characterized by the relatively flatten REE + Y distribution pattern, lower Y/Ho values and high $^{87}Sr/^{86}Sr$ ratios. The calcite veins precipitated from the Early-Middle Ordovician formation water have similar REE + Y compositions, $^{13}C$, $^{18}O$ and $^{87}Sr/^{86}Sr$ isotopic features to those of host rocks. The relationship between the tectonics and fluid flow in the Akeyasu area can be summarized as follows (Fig. 14).

1. During the Middle Caledonian orogeny (approximately 460.9 Ma to 428 Ma), the Ordovician reservoirs in the Akeyasu area experienced uplift and were subjected to atmospheric freshwater weathering and leaching under significant compressive stress (Chen et al., 2022b). This led to the development of Group-I faults. The C1 calcite veins are precipitated from meteoric water during the tectonic uplifts and characterized by the relatively flatten REE + Y distribution pattern, lower Y/Ho values and high $^{87}Sr/^{86}Sr$ ratios. In addition, primary oil inclusions with golden yellow fluorescence colors were observed. Thus, the C1 calcite veins, with a U–Pb age of 459.8 ± 4.7 Ma, primarily derived from meteoric water, precipitated during this phase, coinciding with the first episode of oil charging.
2. During the Late Caledonian orogeny (approximately 420 Ma to 416 Ma), the main faults in the Akeyasu area were reactivated. Meanwhile, the C2 calcite veins were precipitated as a result of fluid flow in the reservoirs caused by tectonics. After extensive fluid-rock interaction, the geochemical properties of Ordovician formation water, including REEs, $\delta^{13}C$, $\delta^{18}O$, and $^{87}Sr/^{86}Sr$ isotopic values, equilibrated with those of the host rocks. The C2 calcite veins (U–Pb age of 418.8 ± 3.7 Ma) inherited these geochemical characteristics.
3. The Early-Middle Hercynian orogeny (approximately 385.3 Ma to 318 Ma) were instrumental in enhancing the physical properties of carbonate reservoirs in the Akeyasu area. These strata underwent significant weathering and erosion due to large-scale tectonic uplift (Han et al., 2019). Due to intense fault activity, Cambrian formation water migrated upward through faults into the Ordovician reservoirs. During this phase, the C3 calcite veins (U–Pb ages ranging from 329.7 ± 1.6 Ma to 310.0 ± 3.6 Ma) with negative Ce anomalies, higher Y/Ho, $^{87}Sr/^{86}Sr$ values and typical REE + Y distribution pattern of marine carbonate rocks were formed. The presence of primary oil inclusions with yellow fluorescence colors in C3 calcite veins indicates the occurrence of the second episode of oil charging during C3 calcite precipitation.

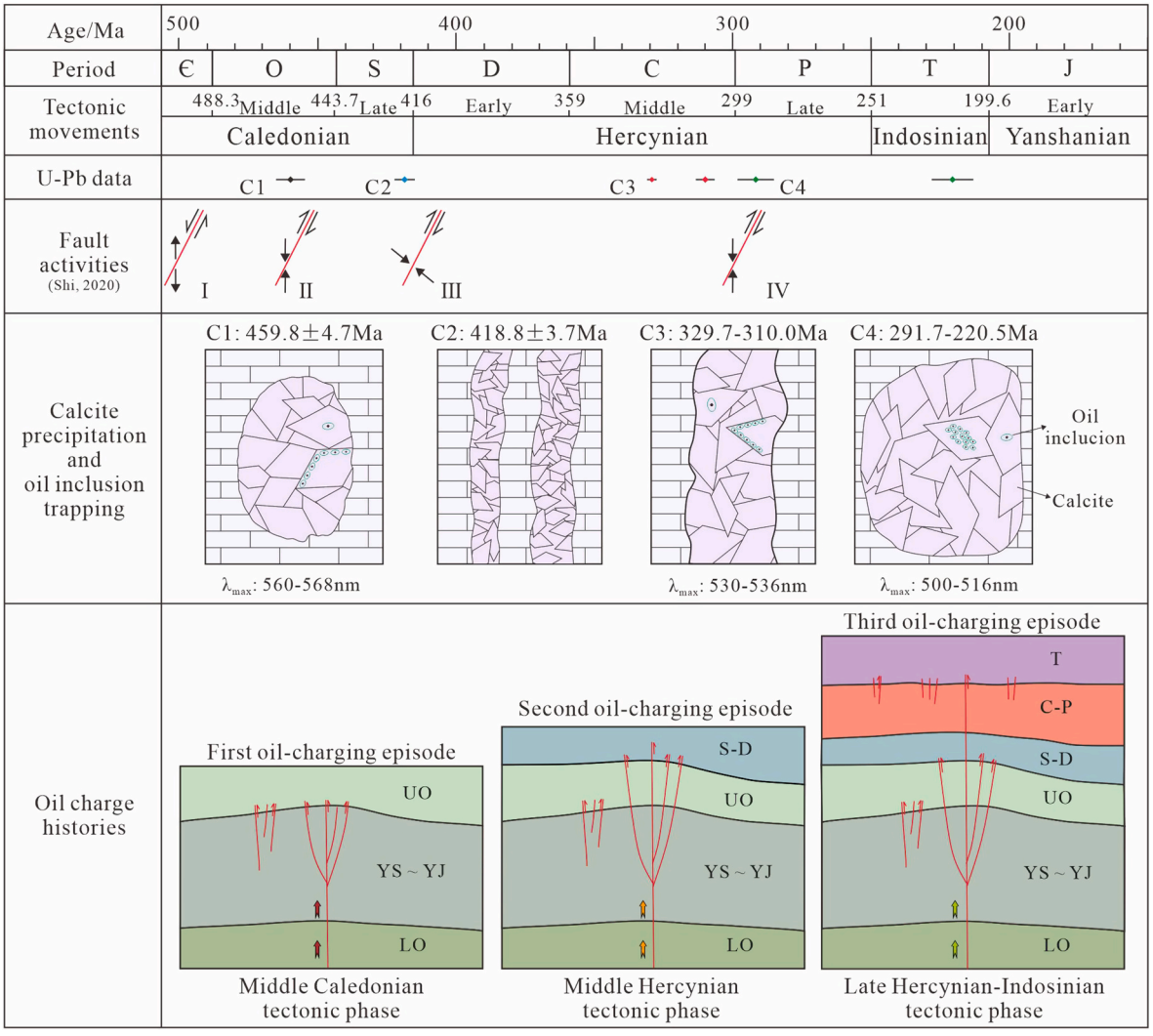


**Fig. 14.** Diagram integrating the tectonic movements, fault activities, calcite precipitation, and oil charge histories in the deeply buried Ordovician reservoirs of the Akeyasu area, Tarim Basin.

4. During the Late Hercynian orogeny (approximately 290 Ma), the Tarim Basin experienced extensive volcanic activity known as the Permian Tarim Large Igneous Province (LIP). U–Pb isotopic ages of the C4 calcite veins (ranging from 291.7 ± 6.1 Ma to 220.5 ± 7.3 Ma) align with the timing of the Tarim LIP (Tian et al., 2010; Zhang et al., 2010; Jin et al., 2013; Zou et al., 2015). The eruption of the Permian mantle plume triggered widespread volcanic activity and fluid flow in the Tarim Basin. The C4 calcite veins derived from hydrothermal fluids exhibit obvious negative Eu anomalies, depletion of $^{18}O$ and symbiosis with fluorite. The higher $^{87}Sr/^{86}Sr$ ratios may be attribute to the clastic layers of Lower Cambrian (Jin et al., 2013; Han et al., 2019). Besides, primary oil inclusions with yellow green (or yellow white) fluorescence colors were detected in C4 calcite veins. Thus, Cambrian clastic material and oil were involved in hydrothermal fluid migration upward along fault systems. These fluids were later injected into the Ordovician reservoirs, resulting in the precipitation of C4 calcite veins. Therefore, the fluid evolution history and oil accumulation process were primarily controlled by orogenies in the deep-burial Ordovician carbonate reservoirs in the Akeyasu area.

## 6. Conclusions

The Tarim Basin has experienced multiple tectonic evolution stages. Multiple phases of calcite veins were developed in association with tectonic history. The calcite veins have distinct petrography, cathodoluminescence, REE + Y compositions, $^{13}C$, $^{18}O$ and $^{87}Sr/^{86}Sr$ isotopic features and U–Pb ages. In-situ U–Pb dating on the calcites with primary oil inclusions can effectively constrain the absolute age of oil charge in superimposed petroliferous basin. The evolution of fluid activity and the process of oil charging within the Akeyasu area were predominantly triggered by regional orogeny, where substantial-scale tectonic events generated intensive faulting activities that, in turn, regulated fluid dynamics and exerted a notable influence on both calcite precipitation and oil charging processes. Thus, the petroleum migration and accumulation in multistage tectonically superimposed basins often occurred concurrently with the fluid activity events, which is closely associated with regional orogeny. This study combined tectonic geochronology and fluid evolution analysis, addressed the fluid flow process and hydrocarbon charge history in deeply buried carbonate reservoirs that may aid in further understanding the petroleum accumulation process in the multistage tectonically superimposed basins.

## CRediT authorship contribution statement

**Hao Xu:** Data curation, Investigation, Methodology, Writing – original draft. **Zicheng Cao:** Data curation, Writing – review & editing, Project administration. **Lili Gui:** Formal analysis, Investigation, Methodology. **Kamaldeen O. Omosanya:** Writing – review & editing. **Feng Geng:** Project administration, Writing – review & editing. **Ze Tao:** Data curation, Writing – review & editing. **Xiaowen Guo:** Funding acquisition, Writing – review & editing.

## Declaration of competing interest

The authors declare that they have no known competing financial interests or personal relationships that could have appeared to influence the work reported in this paper.

## Data availability

Data will be made available on request.

## Acknowledgement

This study was supported by the Joint Funds of the National Natural Science Foundation of China (No. U20B6001). The SINOPEC Northwest Oilfield is thanked for providing background geological data and samples. We would like to express special thanks to the MPG chief editor Qinhong Hu and associate editor Davide Lenaz for handling our manuscript, David Cruset and another anonymous reviewer for their constructive comments and suggestions.

## References

Alexander, B.W., Bau, M., Andersson, P., Dulski, P., 2008. Continentally-derived solutes in shallow Archean seawater: rare earth element and Nd isotope evidence in iron formation from the 2.9Ga Pongola Supergroup, South Africa. Geochem. Cosmochim. Acta 72, 378–394. https://doi.org/10.1016/j.gca.2007.10.028.

Alibert, C., McCulloch, M.T., 1993. Rare earth element and neodymium isotopic compositions of the banded iron-formations and associated shales from Hamersley, western Australia. Geochem. Cosmochim. Acta 57, 187–204. https://doi.org/10.1016/0016-7037(93)90478-F.

Banner, J.L., 2004. Radiogenic isotopes: systematics and applications to earth surface processes and chemical stratigraphy. Earth Sci. Rev. 65, 141–194. https://doi.org/10.1016/S0012-8252(03)00086-2.

Banner, J.L., Hanson, G.N., 1990. Calculation of simultaneous isotopic and trace element variations during water-rock interaction with applications to carbonate diagenesis. Geochem. Cosmochim. Acta 54 (11), 3123–3137. https://doi.org/10.1016/0016-7037(90)90128-8.

Bau, M., 1991. Rare-earth element mobility during hydrothermal and metamorphic fluid-rock interaction and the significance of the oxidation state of europium. Chem. Geol. 93, 219–230. https://doi.org/10.1016/0009-2541(91)90115-8.

Bau, M., Dulski, P., 1996. Distribution of yttrium and rare-earth elements in the penge and kuruman iron-formations, transvaal supergroup, South Africa. Precambrian Res. 79, 37–55. https://doi.org/10.1016/0301-9268(95)00087-9.

Bolhar, R., Kamber, B.S., Moorbath, S., Fedo, C.M., Whitehouse, M.J., 2004. Characterisation of early Archaean chemical sediments by trace element signatures. Earth Planet Sci. Lett. 222, 43–60. https://doi.org/10.1016/j.epsl.2004.02.016.

Bolhar, R., Van Kranendonk, M.J., 2007. A non-marine depositional setting for the northern Fortescue Group, Pilbara Craton, inferred from trace element geochemistry of stromatolitic carbonates. Precambrian Res. 155, 229–250. https://doi.org/10.1016/j.precamres.2007.02.002.

Caja, M.A., Permanyer, A., Marfil, R., 2006. Oil migration and its influence in fracture-fill cementation (south-eastern pyrenees, spain): geochemistry and fluid inclusion evidence. In: 10th ALAGO Congress on Organic Geochemistry.

Cao, R., Zhao, H., Lan, Z., 2023. Calcite U-Pb geochronology revealing late ediacaran–early paleozoic hydrothermal alteration in the stenian-tonian carbonate of northeastern north China craton. J. Earth Sci. 34 (6), 1724–1731. https://doi.org/10.1007/s12583-023-1859-6.

Chen, J., Guo, X., Tao, Z., Cao, Z., Wang, B., Zhang, X., Xu, H., Zhao, J.-x., 2022a. U-Pb dating of oil charge in superimposed basins: a case study from the Tarim Basin, NW China. GSA Bull 134, 3176–3188. https://doi.org/10.1130/b36324.1.

Chen, L., Zhang, H., Cai, Z., Hao, F., Xue, Y., Zhao, W., 2022b. Petrographic, mineralogical and geochemical constraints on the fluid origin and multistage karstification of the Middle-Lower Ordovician carbonate reservoir, NW Tarim Basin, China. J. Petrol. Sci. Eng. 208 https://doi.org/10.1016/j.petrol.2021.109561.

Cong, F., Tian, J., Hao, F., Kylander-Clark, A.R.C., Pan, W., Zhang, B., 2022. Calcite U-Pb ages constrain petroleum migration pathways in tectonic complex basins. Geology 50, 644–649. https://doi.org/10.1130/g49750.1.

Coogan, L.A., Parrish, R.R., Roberts, N.M.W., 2016. Early hydrothermal carbon uptake by the upper oceanic crust: insight from in situ U-Pb dating. Geology 44, 147–150. https://doi.org/10.1130/g37212.1.

Cruset, D., Vergés, J., Muñoz-López, D., Moragas, M., Cantarero, I., Travé, A., 2023. Fluid evolution from extension to compression in the pyrenean fold belt and Basque-cantabrian basin: a review. Earth Sci. Rev. 243, 104494 https://doi.org/10.1016/j.earscirev.

Cruset, D., Vergés, J., Rodrigues, N., Belenguer, J., Pascual-Cebrian, E., Almar, Y., Pérez-Cáceres, I., Macchiavelli, C., Travé, A., Beranoaguirre, A., Albert, R., Gerdes, A., Messager, G., 2021. U–Pb dating of carbonate veins constraining timing of beef growth and oil generation within Vaca Muerta Formation and compression history in the Neuquén Basin along the Andean fold and thrust belt. Mar. Petrol. Geol. 132, 105204 https://doi.org/10.1016/j.marpetgeo.2021.

Deng, S., Zhao, R., Kong, Q., Li, Y., Li, B., 2022. Two distinct strike-slip fault networks in the Shunbei area and its surroundings, Tarim Basin: hydrocarbon accumulation, distribution, and controlling factors. AAPG (Am. Assoc. Pet. Geol.) Bull. 106 (1), 77–102. https://doi.org/10.1306/07202119113.

Dewever, B., Berwouts, I., Swennen, R., Breesch, L., Ellam, R.M., 2010. Fluid flow reconstruction in karstified Panormide platform limestones (north-central Sicily): implications for hydrocarbon prospectivity in the Sicilian fold and thrust belt. Mar. Petrol. Geol. 27, 939–958. https://doi.org/10.1016/j.marpetgeo.2009.10.018.

German, C.R., Elderfield, H., 1989. Rare earth elements in Saanich Inlet, British Columbia, a seasonally anoxic basin. Geochem. Cosmochim. Acta 53, 2561–2571. https://doi.org/10.1016/0016-7037(89)90128-2.

Guilhaumou, N., Szydlowskii, N., Pradier, B., 1990. Characterization of hydrocarbon fluid inclusions by infra-red and fluorescence microspectrometry. Mineral. Mag. 54, 311–324. https://doi.org/10.1180/minmag.1990.054.375.17.

Guo, X., Liu, K., Jia, C., Song, Y., Zhao, M., Lu, X., 2016. Effects of early petroleum charge and overpressure on reservoir porosity preservation in the giant Kela-2 gas field,

Kuqa depression, Tarim Basin, northwest China. AAPG (Am. Assoc. Pet. Geol.) Bull. 100, 191–212. https://doi.org/10.1306/11181514223.
Hagemann, H.W., Hollerbach, A., 1986. The fluorescence behaviour of crude oils with respect to their thermal maturation and degradation. Org. Geochem. 10, 473–480. https://doi.org/10.1016/0146-6380(86)90047-1.
Han, C., Lin, C., Lu, X., Tian, J., Ren, L., Ma, C., 2019. Petrological and geochemical constraints on fluid types and formation mechanisms of the Ordovician carbonate reservoirs in Tahe Oilfield, Tarim Basin, NW China. J. Petrol. Sci. Eng. 178, 106–120. https://doi.org/10.1016/j.petrol.2019.03.010.
Hanson, A.D., Zhang, S.C., Moldowan, J.M., Liang, D.G., Zhang, B.M., 2000. Molecular organic geochemistry of the Tarim Basin, northwest China. AAPG (Am. Assoc. Pet. Geol.) Bull. 84, 1109–1128. https://doi.org/10.1306/A9673C52-1738-11D7-8645000102C1865D.
He, Z.L., Ding, Q., Wo, Y.J., Zhang, J.T., Fan, M., Yue, X.J., 2017. Experiment of Carbonate Dissolution: implication for high quality carbonate reservoir formation in deep and ultradeep basins. Geofluids 1–8, 2017.
He, Z.L., Li, S.j., Li, Y.q., Gao, J., 2022. Multi-directional and multiphase tectonic modification, and hydrocarbon differential enrichment in the middle-upper yangtze regio. J. Earth Sci. 33, 1246–1259.
He, Z.L., Sun, J.F., Guo, P.H., Wei, H.H., Lyu, X.R., Han, K.L., 2021. Construction of carbonate reservoir knowledge base and its application in fracture-cavity reservoir geological modeling. Petrol. Explor. Dev. 48, 824–834.
Hooker, J.N., Cartwright, J., Stephenson, B., Silver, C.R.P., Dickson, A.J., Hsieh, Y.-T., 2017. Fluid evolution in fracturing black shales, Appalachian Basin. AAPG (Am. Assoc. Pet. Geol.) Bull. 101, 1203–1238. https://doi.org/10.1306/10031616030.
Hu, S., Wilkes, H., Horsfield, B., Chen, H., Li, S., 2016. On the origin, mixing and alteration of crude oils in the Tarim Basin. Organic Geochem. 97, 17–34. https://doi.org/10.1016/j.orggeochem.2016.04.005.
Huang, S.J., Liu, S.G., Li, G.R., Zhang, M., Wu, W.H., 2004. Strontium isotope composition of marine carbonate and the influence of diagenetic fluid on it in ordovician. J. Chengdu Univ. Technol. (Sci. Technol. Ed.) 1–7 (in Chinese with English abstract).
Jia, C.Z., Wei, G.Q., 2002. Structural characteristics and petroliferous features of Tarim Basin. Chin. Sci. Bull. 47, 1–11. https://doi.org/10.1007/BF02902812.
Jia, L., Cai, C., Li, K., Liu, L., Chen, Z., Tan, X., 2022. Impact of fluorine-bearing hydrothermal fluid on deep burial carbonate reservoirs: a case study from the Tazhong area of Tarim Basin, northwest China. Mar. Petrol. Geol. 139, 105579 https://doi.org/10.1016/j.marpetgeo.
Jin, Z., Liu, Q., Yun, J., 2016. Potential petroleum sources and exploration directions around the Manjar Sag in the Tarim Basin. Sci. China Earth Sci. 60, 235–245. https://doi.org/10.1007/s11430-015-5573-7.
Jin, Z.J., Zhu, Y.D., Meng, Q.Q., Hu, W.X., 2013. Hydrothermal activites and influences on migration of oil and gas in Tarim Basin. Acta Pet. Sin. 29, 1048–1058 (in Chinese with English abstract).
Johannessen, K.C., Vander Roost, J., Dahle, H., Dundas, S.H., Pedersen, R.B., Thorseth, I. H., 2017. Environmental controls on biomineralization and Fe-mound formation in a low-temperature hydrothermal system at the Jan Mayen Vent Fields. Geochem. Cosmochim. Acta 202, 101–123. https://doi.org/10.1016/j.gca.2016.12.016.
Kerans, C., 1988. Karst-controlled reservoir heterogeneity in ellenburger group carbonates of west Texas1. AAPG (Am. Assoc. Pet. Geol.) Bull. 72, 1160–1183. https://doi.org/10.1306/703C996F-1707-11D7-8645000102C1865D.
Klein, C., Beukes, N.J., 1989. Geochemistry and sedimentology of a facies transition from limestone to iron-formation deposition in the early Proterozoic Transvaal Supergroup, South Africa. Econ. Geol. 84, 1733–1774. https://doi.org/10.2113/gsecongeo.84.7.1733.
Lawrence, M.G., Greig, A., Collerson, K.D., Kamber, B.S., 2006. Rare earth element and yttrium variability in south east Queensland waterways. Aquat. Geochem. 12, 39–72. https://doi.org/10.1007/s10498-005-4471-8.
Lei, Q., Xu, Y., Yang, Z., Cai, B., Wang, X., Zhou, L., Liu, H., Xu, M., Wang, L., Li, S., 2021. Progress and development directions of stimulation techniques for ultra-deep oil and gas reservoirs. Petrol. Explor. Dev. 48, 221–231. https://doi.org/10.1016/s1876-3804(21)60018-6.
Li, Q., Parrish, R.R., Horstwood, M.S.A., McArthur, J.M., 2014. U–Pb dating of cements in Mesozoic ammonites. Chem. Geol. 376, 76–83. https://doi.org/10.1016/j.chemgeo.2014.03.020.
Liu, C.G., Li, G.R., Zhu, C.L., Liu, G.Y., Lu, Y.F., 2008. Geochemistry characteristics of carbon, oxygen and strontium isotopes of calcites filled in karstic fissure-cave in lower-middle ordovician of Tahe oilfield , Tarim Basin. Earth Sci. 33, 377–386 (in Chinese with English abstract).
Liu, E., Zhao, J.-X., Wang, H., Pan, S., Feng, Y., Chen, Q., Liu, F., Xu, J., 2021. LA-ICPMS in-situ U-Pb geochronology of low-uranium carbonate minerals and its application to reservoir diagenetic evolution studies. J. Earth Sci. 32 (4), 872–879. https://doi.org/10.1007/s12583-020-1084-5.
Liu, Shiju, Gao, Gang, Wenzhe, Gang, Xiang, Baoli, Wang, Ming, Wang, Chengyun, 2023. Comparison of formation conditions of source rocks of fengcheng and lucaogou formations in the junggar basin, NW China: implications for organic matter enrichment and hydrocarbon potential. J. Earth Sci. 34 (4), 1026–1040. https://doi.org/10.1007/s12583-021-1566-0.
Lottermoser, B.G., 1992. Rare earth elements and hydrothermal ore formation processes. Ore Geol. Rev. 7, 25–41. https://doi.org/10.1016/0169-1368(92)90017-F.
McArthur, J.M., Howarth, R.J., Bailey, T.R., 2001. Strontium isotope stratigraphy: LOWESS version 3: best fit to the marine Sr-isotope curve for 0–509 Ma and accompanying look-up table for deriving numerical age. J. Geol. 109, 155–170.
McArthur, J.M., Kennedy, W.J., Gale, A.S., Thirlwall, M.F., Chen, M., Burnett, J., Hancock, J.M., 1992. Strontium isotope stratigraphy in the Late Cretaceous: intercontinental correlation of the Campanian/Maastrichtian boundary. Terra. Nova 4, 385–393. https://doi.org/10.1111/j.1365-3121.1992.tb00827.x.
McArthur, J.M., 1994. Recent trends in strontium isotope stratigraphy. Terra. Nova 6, 331–358. https://doi.org/10.1111/j.1365-3121.1994.tb00507.x.
Moore, C.H., Wade, W.J., 2013. Carbonate reservoirs porosity and diagenesis in a sequence stratigraphic framework, 2. impr. In: Devel. Sedim. 67. Elsevier, New York.
Nuriel, P., Weinberger, R., Kylander-Clark, A.R.C., Hacker, B.R., Craddock, J.P., 2017. The onset of the Dead Sea transform based on calcite age-strain analyses. Geology 45, 587–590. https://doi.org/10.1130/g38903.1.
Palmer, M., Elderfield, H., 1985. Sr isotope composition of sea water over the past 75 Myr. Nature 314, 526–528. https://doi.org/10.1038/314526a0.
Ping, H., Chen, H., George, S.C., 2020. Quantitatively predicting the thermal maturity of oil trapped in fluid inclusions based on fluorescence and molecular geochemical data of oil inclusions in the Dongying depression, Bohai Bay Basin, China. AAPG (Am. Assoc. Pet. Geol.) Bull. 104, 1751–1791. https://doi.org/10.1306/09271919096.
Rochelle-Bates, N., Roberts, N.M.W., Sharp, I., Freitag, U., Verwer, K., Halton, A., Fiordalisi, E., van Dongen, B.E., Swart, R., Ferreira, C.H., Dixon, R., Schröder, S., 2020. Geochronology of volcanically associated hydrocarbon charge in the pre-salt carbonates of the Namibe Basin, Angola. Geology 49 (3), 335–340. https://doi.org/10.1130/g48019.1.
Roberts, N.M.W., Walker, R.J., 2016. U-Pb geochronology of calcite-mineralized faults: absolute timing of rift-related fault events on the northeast Atlantic margin. Geology 44, 531–534. https://doi.org/10.1130/g37868.1.
Shi, J.X., 2020. Study on Controlling Effects of Faults and Fractures on Ordovician Carbonate Fracture-Cavity Bodies in Tahe Oilfield. Ph.D. thesis, China Univ. Petrol., Beijing, China, p. 12 (in Chinese with English abstract).
Shields, G., Stille, P., 2001. Diagenetic constraints on the use of cerium anomalies as palaeoseawater redox proxies: an isotopic and REE study of Cambrian phosphorites. Chem. Geol. 175, 29–48. https://doi.org/10.1016/S0009-2541(00)00362-4.
Shields, G.A., Carden, G.A.F., Veizer, J., Meidla, T., Rong, J.-Y., Li, R.-Y., 2003. Sr, C, and O isotope geochemistry of Ordovician brachiopods: a major isotopic event around the Middle-Late Ordovician transition. Geochem. Cosmochim. Acta 67, 2005–2025. https://doi.org/10.1016/S0016-7037(02)01116-X.
Smith, P.E., Farquhar, R.M., Hancock, R.G., 1991. Direct radiometric age determination of carbonate diagenesis using U-Pb in secondary calcite. Earth Planet Sci. Lett. 105, 474–491. https://doi.org/10.1016/0012-821X(91)90186-L.
Sun, H., Sun, X., Wei, X., Huang, X., Ke, G., Wei, H., 2023. Geochemical characteristics and origin of nuanquanzi geothermal water in yudaokou, chengde, hebei, north China. J. Earth Sci. 34 (3), 838–856.
Tao, Z., He, Z., Alves, T.M., Guo, X., Gao, J., He, S., Zhao, W., 2022. Structural inheritance and its control on overpressure preservation in mature sedimentary basins (Dongying depression, Bohai Bay Basin, China). Mar. Petrol. Geol. 137 https://doi.org/10.1016/j.marpetgeo.2021.105504.
Taylor, S.R., McLennan, S.M., 1985. The continental crust: its composition and evolution. Blackwell Scientific Publications, Oxford 57 (114), 230–372, 143–209.
Tian, F., Jin, Q., Lu, X., Lei, Y., Zhang, L., Zheng, S., Zhang, H., Rong, Y., Liu, N., 2016. Multi-layered ordovician paleokarst reservoir detection and spatial delineation: a case study in the Tahe Oilfield, Tarim Basin, Western China. Mar. Petrol. Geol. 69, 53–73. https://doi.org/10.1016/j.marpetgeo.2015.10.015.
Tian, W., Campbell, I.H., Allen, C.M., Guan, P., Pan, W., Chen, M., Yu, H., Zhu, W., 2010. The Tarim picrite–basalt–rhyolite suite, a Permian flood basalt from northwest China with contrasting rhyolites produced by fractional crystallization and anatexis. Contrib. Mineral. Petrol. 160, 407–425. https://doi.org/10.1007/s00410-009-0485-3.
Van Kranendonk, M.J., Webb, G.E., Kamber, B.S., 2003. Geological and trace element evidence for a marine sedimentary environment of deposition and biogenicity of 3.45 Ga stromatolitic carbonates in the Pilbara Craton, and support for a reducing Archaean ocean. Geobiology 1, 91–108. https://doi.org/10.1046/j.1472-4669.2003.00014.x.
Veizer, J., Ala, D., Azmy, K., Bruckschen, P., Buhl, D., Bruhn, F., Carden, G.A.F., Diener, A., Ebneth, S., Godderis, Y., Jasper, T., Korte, C., Pawellek, F., Podlaha, O.G., Strauss, H., 1999. 87Sr/86Sr, δ13C and δ18O evolution of Phanerozoic seawater. Chem. Geol. 161, 59–88. https://doi.org/10.1016/S0009-2541(99)00081-9.
Wang, S., Liu, H., Wu, X., Cheng, B., Zhao, S., 2023. Major period and process of hydrocarbon accumulation of deep reservoirs — a case study of Tuoputai area in Tarim Basin, China. J. Petrol. Sci. Eng. 221 https://doi.org/10.1016/j.petrol.2022.111305.
Wang, Z., Zhang, Y., Tao, X., Zhu, B., Luo, C., 2014. Genesis of the Ordovician fluorite and its geological significance in central uplift of the Tarim basin, China. Mineral. Petrol. 109 (3), 339–348. https://doi.org/10.1007/s00710-014-0341-7.
Wu, L., Jin, Z., Liu, K., Chu, Z., Yang, P., 2021. Evolution of a deeply-buried oil reservoir in the north Shuntuoguole Low Uplift, Tarim Basin, western China: insights from molecular geochemistry and Re–Os geochronology. Mar. Petrol. Geol. 134 https://doi.org/10.1016/j.marpetgeo.2021.105365.
Xu, H., Guo, X., Cao, Zi, C., Wang, B., Liu, Y., Chen, J., Zhang, X., Luo, T., 2021. Application of minimum homogenization temperatures of aqueous inclusions in calcite veins to determine the time of hydrocarbon accumulation in the Ordovician of Tahe Oilfield: evidence from the in-suit calcite U-Pb dating by laser ablation. Earth Sci. 46 (10), 3535–3548 (in Chinese with English abstract).
Yang, P., Liu, K., Li, Z., Rankenburg, K., McInnes, B.I.A., Liu, J., Evans, N.J., 2022a. Direct dating Paleo-fluid flow events in sedimentary basins. Chem. Geol. 120642 588. https://doi.org/10.1016/j.chemgeo.
Yang, P., Liu, K., Li, Z., McInnes, B.I.A., Liu, J., 2022b. Evolution of ordovician YJ1X ultra-deep oil reservoir in the yuecan oilfield, Tarim Basin, NW China. Petrol. Explor. Dev. 49 (2), 300–312. https://doi.org/10.1016/s1876-3804.

Yun, L., 2008. Petroleum Accumulation Model of Ordovician Reservoir in Tahe Oilfield. Ph.D. thesis, China Univ. Geosci., Wuhan, China, p. 15 (in Chinese with English abstract).

Zhao, Y.Y., Li, S.Z., Li, D., Guo, L.L., Dai, L.M., Tao, J.L., 2019. Rare earth element geochemistry of carbonate and its paleoenvironmental implications. Geotect. Metallogenia 43, 141–167 (in Chinese with English abstract).

Zhang, C.-L., Li, Z.-X., Li, X.-H., Xu, Y.-G., Zhou, G., Ye, H.-M., 2010. A Permian large igneous province in Tarim and Central Asian orogenic belt, NW China: results of a ca. 275 Ma mantle plume? GSA Bull 122, 2020–2040. https://doi.org/10.1130/B30007.1.

Zhang, S., Huang, H., 2005. Geochemistry of Palaeozoic marine petroleum from the Tarim Basin, NW China: Part 1. Oil family classification. Org. Geochem. 36, 1204–1214. https://doi.org/10.1016/j.orggeochem.2005.01.013.

Zhu, G., Milkov, A.V., Zhang, Z., Sun, C., Zhou, X., Chen, F., Han, J., Zhu, Y., 2019. Formation and preservation of a giant petroleum accumulation in superdeep carbonate reservoirs in the southern Halahatang oil field area. Tarim Basin, China. AAPG (Am. Assoc. Pet. Geol.) Bull. 103, 1703–1743. https://doi.org/10.1306/11211817132.

Zong, K., Klemd, R., Yuan, Y., He, Z., Guo, J., Shi, X., Liu, Y., Hu, Z., Zhang, Z., 2017. The assembly of Rodinia: the correlation of early Neoproterozoic (ca. 900 Ma) high-grade metamorphism and continental arc formation in the southern Beishan Orogen, southern Central Asian Orogenic Belt (CAOB). Precambrian Res. 290, 32–48. https://doi.org/10.1016/j.precamres.2016.12.010.

Zou, S.-Y., Li, Z.-L., Song, B., Ernst, R.E., Li, Y.-Q., Ren, Z.-Y., Yang, S.-F., Chen, H.-L., Xu, Y.-G., Song, X.-Y., 2015. Zircon U–Pb dating, geochemistry and Sr–Nd–Pb–Hf isotopes of the Wajilitag alkali mafic dikes, and associated diorite and syenitic rocks: implications for magmatic evolution of the Tarim large igneous province. Lithos 212–215, 428–442. https://doi.org/10.1016/j.lithos.2014.09.005.